



# Sr(Sn,Se)O<sub>3</sub> modified Bi<sub>0.5</sub>K<sub>0.5</sub>TiO<sub>3</sub> ferroelectric ceramics: structural, electrical and leakage current characteristics

B. B. Arya<sup>1</sup> · N. P. Samantray<sup>1</sup> · R. N. P. Choudhary<sup>1</sup>

Received: 29 September 2022 / Accepted: 5 December 2022 / Published online: 23 December 2022  
© The Author(s), under exclusive licence to Springer-Verlag GmbH, DE part of Springer Nature 2022

## Abstract

This research article deliberates the structural, electrical and leakage current characteristics of strontium stannate- selenites, (Sr(Sn,Se)O<sub>3</sub>) modified bismuth potassium titanate (Bi<sub>0.5</sub>K<sub>0.5</sub>TiO<sub>3</sub>) compound of chemical compositions (1-2x) (Bi<sub>0.5</sub>K<sub>0.5</sub>) TiO<sub>3-x</sub> (SrSnO<sub>3</sub>)-x (SrSeO<sub>3</sub>) (x=0, 0.05, 0.10, 0.15). The compounds have been synthesized through a solid-state reaction process with calcination temperature = 1000 °C and sintering temperature = 1050 °C for 5 h each. The room temperature XRD spectrum indicates the development of single-phase ceramics with tetragonal symmetry. Detailed investigations of the electrical characteristics as a function of frequency (1 kHz to 1 MHz) and temperature (25–500 °C) are obtained using the programmable phase-sensitive meter. The leakage current (J–E) properties of the materials have shown a very small amount of leakage current density with the existence of an Ohmic conduction mechanism. The room temperature polarization study through the hysteresis loops confirms the ferroelectric properties of the studied materials. The remarkable experimental results obtained here suggest the usefulness of the prepared materials in various electronic devices.

**Keywords** XRD spectrum · Single-phase · Leakage current · Ohmic conduction · Ferroelectric

## 1 Introduction

Lead zirconate titanate, Pb(Zr,Ti)O<sub>3</sub> (PZT), has been recognized as a lead-based piezoelectric compound, with a perovskite structure. Because of their excellent piezoelectric (i.e., large piezoelectric constant and high-temperature stability) and electrical characteristics, they have widely been used in the application of different electronic devices including sensors, actuators, resonators, transducers, transformers, wave filters, hydrophones, etc. [1]. PZT exhibits a remarkable phase boundary that separates the region with tetragonal and rhombohedral symmetry called the MPB (morphotropic phase boundary) as reported by Jaffe et al. [2]. Above the Curie point ( $T_c = 350$  °C), the unit cell of PZT shows a simple cubic structure and does not show the ferroelectric and electric properties but below  $T_c$ , it shows either rhombohedral (Zr-rich) or tetragonal (Ti-rich) symmetry depending upon the concentration of Zr and Ti. The zirconium-rich rhombohedral phase shows the two space

groups,  $R3m$  and  $R3c$  and the titanium-rich tetragonal phase has a space group,  $P4mm$  [3]. Although PZT has so many advantages, but the toxic evaporation of lead oxide at the time of sintering caused severe environmental pollution, and this is also associated with the use as well as the disposal of the components [4]. Hence, in recent years, significant attention has been provided to the use of lead-free piezoelectric and ferroelectric compounds as an alternative to overcome these problems. Among the lead-free ferroelectric compounds, bismuth potassium titanate (Bi<sub>0.5</sub>K<sub>0.5</sub>TiO<sub>3</sub>) (abbreviated as BKT) has been taken as the most promising candidate for device applications because of its excellent ferroelectric and related properties. BKT shows a stable perovskite structure with a comparatively high Curie temperature ( $T_c = 380$  °C–420 °C) than that of Bi<sub>0.5</sub>Na<sub>0.5</sub>TiO<sub>3</sub> (320 °C). Hence, this material has been used in different applications including resonators, micro-electro-mechanical systems (MEMS), filters, etc. [5]. BKT shows a tetragonal crystal structure (point group,  $4mm$ ) having unit cell parameters,  $a = 3.941$  Å,  $c = 4.000$  Å [6]. The piezoelectric, dielectric, and ferroelectric properties of BKT were reported by Hiruma et al. [7] such as the dielectric constant  $\epsilon_r = 770$ , the remnant polarization ( $P_r$ ) = 22.2 µC/cm, as well as a coercive field ( $E_c$ ) = 52.5 kV/cm. However, BKT shows some

✉ B. B. Arya  
bbarya96@gmail.com

<sup>1</sup> Department of Physics, Siksha 'O' Anusandhan, Deemed to be university, Bhubaneswar, Odisha, India

disadvantages including high electrical conductivity and a large coercive field ( $E_c$ ), which cause difficulty in poling process of the ceramic. To overcome this problem, the substitution of some other compounds is made in the pure BKT to enhance its ferroelectric and other electrical properties [8]. In the present work,  $\text{SrSnO}_3$  and  $\text{SrSeO}_3$  have been added in equal amounts (i.e., in 5%, 10%, and 15%) to the parent BKT sample to study the change in the physical properties of the compound.  $\text{SrSnO}_3$  (SSn) belongs to alkaline earth stannates, which are widely used in the fields of industries and technical applications such as chemical sensors, humidity sensors, gas sensors, semiconductor sensors, Li-ion batteries, antistatic coatings, etc. SSn is considered as a wide band gap (4–5 eV) semiconductor with low effective mass [9]. SSn shows three non-cubic polymorphs such as (i) orthorhombic phase (space group, Pnma) at room temperature, (ii) orthorhombic phase (space group, Imma) at  $632^\circ\text{C} < T < 789^\circ\text{C}$ , and (iii) tetragonal phase (space group, I4/mcm) at  $T > 789^\circ\text{C}$  [10]. The room temperature orthorhombic crystal system (space group, Pnma) shows the lattice parameters;  $a = 5.717 \text{ \AA}$ ,  $b = 5.729 \text{ \AA}$ ,  $c = 8.084 \text{ \AA}$  [11]. Similarly,  $\text{SrSeO}_3$  (SSe) belongs to the family of alkaline earth selenites having the standard formula  $\text{XSeO}_3$  ( $X = \text{Ba, Sr, Ca}$ ) and has also drawn great attention from researchers due to its attractive ferroelectric properties. The selenium compounds having 4+ oxidation states comprise versatile applications according to their practice as well as scientific value. These compounds are used in the fields of electronic industries, agriculture organic synthesis, medicine, glass industries, chemical laboratories, etc. [12]. The metal selenites which possess transition metals with  $d^0$  electronic configuration have widely been taken for research because of their potential applications in the field of photoelectric materials, such as piezoelectric ceramics, second-order NLO (nonlinear optical) compounds, and pyroelectric [13].  $\text{SrSeO}_3$  exhibits a monoclinic centrosymmetric structure (space group,  $P2_1/m$ ) with the cell constant;  $a = 4.456(1) \text{ \AA}$ ,  $b = 5.478(1) \text{ \AA}$ ,  $c = 6.574(1) \text{ \AA}$ ,  $\beta = 107.34(1)^\circ$ , cell volume ( $V$ ) =  $153.2(1) \text{ \AA}^3$ , (where the number in parenthesis is the standard deviation), calculated density ( $\rho_{\text{cal}}$ ) =  $4.65 \text{ g/cm}^3$  and coordination number  $Z = 2$ . Here,  $\text{Sr}^{2+}$  cations are of ninefold coordination with the average bond length of  $\text{Sr-O} = 2.741 \text{ \AA}$ . [14]. The  $\text{SeO}_2$ -containing glass possesses high ionic conductivity at room temperature (i.e.,  $10^{-3}$ – $10^{-4} \text{ S/cm}$ ) due to the high value of polarizability of the selenium ion [15]. The complex composition of  $\text{SeO}_2$  glasses acts as a potential candidate for technical applications including super ionic semiconductors, nonlinear optical devices, reflecting windows, sensors, soluble micro-fertilizers, infrared transmission components, etc. The major benefit of introducing  $\text{SeO}_2$  to glass composition is its capability of decreasing the melting point of the compositions and modifying the optical properties [16]. Considering

the above remarkable results of SSn and SSe, in this work we have synthesized the  $\text{Sr}(\text{Sn,Se})\text{O}_3$  modified  $(\text{Bi}_{0.5}\text{K}_{0.5})\text{TiO}_3$  ceramics. The electrical, ferroelectric, and leakage current characteristics of the pure BKT ceramics have been improved extensively with the addition of an equivalent amount of SSn-SSe to it.

## 2 Experimental

$\text{Sr}(\text{Sn,Se})\text{O}_3$  modified  $(\text{Bi}_{0.5}\text{K}_{0.5})\text{TiO}_3$  polycrystalline compounds with a chemical composition  $(1-2x) [(\text{Bi}_{0.5}\text{K}_{0.5})\text{TiO}_3] + x (\text{SrSnO}_3) + x (\text{SrSeO}_3)$  (i.e., BKT-SSn-SSe) with  $x = 0, 0.05, 0.10$  and  $0.15$  have been prepared through a cost-effective mixed oxide reaction route. The AR grade oxides and carbonates such as  $\text{Bi}_2\text{O}_3$  (99.0%),  $\text{K}_2\text{CO}_3$  (>98%),  $\text{TiO}_2$  (99.5%),  $\text{SrCO}_3$  (99.9%),  $\text{SnO}_2$  (99.9%) all from M/s Loba Chemie Co Ltd and  $\text{SeO}_2$  (>98%) from M/S Merck-Schuchardt were stoichiometrically taken by high precision digital balance and systematically mixed in an agate mortar and pestle in both dry and wet grinding mode for 4 h each. The homogeneously mixed powders were calcined at  $1000^\circ\text{C}$  for 5 h in a high-temperature muffle furnace by using a cylindrical alumina crucible (M/S ANTS ceramics).

As some parts of bismuth oxide may get evaporated at high temperatures, 2% of extra  $\text{Bi}_2\text{O}_3$  was taken to compensate for the loss (if any) during the synthesis. The calcinated samples were ground to a fine powder and while preparing cylindrical pellets, they were homogeneously combined with a few drops of PVA (binder) solution for better binding. The cylindrical pellets with a diameter of around 12 mm and thickness of around 1–2 mm were formed using a KBr press at a hydraulic pressure of  $4 \times 10^5 \text{ N/m}^2$ . The prepared pellets were sintered in a muffle furnace at  $1050^\circ\text{C}$  for 5 h. The room temperature X-ray spectrum of the calcined powders was carried out through the diffraction data recorded from the Rigaku Ultima IV diffractometer having  $\text{CuK}\alpha$  radiation with  $\lambda = 1.5405 \text{ \AA}$  to give information regarding the crystal structure. A thin coating of silver paint was done on the two opposite surfaces of pellets and heated at  $150^\circ\text{C}$  for 2 h before the electrical measurements of the samples. The phase-sensitive meter (N4L model PSM 1735) was used for different electrical measurements and the data were recorded within 1 kHz–1 MHz of frequency and  $25^\circ\text{C}$ – $500^\circ\text{C}$  of temperature. J-E characteristics of the compounds were verified by using an electrometer (Keithley, model 6517B). P-E loop tracer (Marine India) was used to trace the room temperature hysteresis loops of the samples. For detailed information about the experimental procedure, the schematic diagram of the experimental configuration of the solid-state reaction method and characterization is given in Fig. 1.

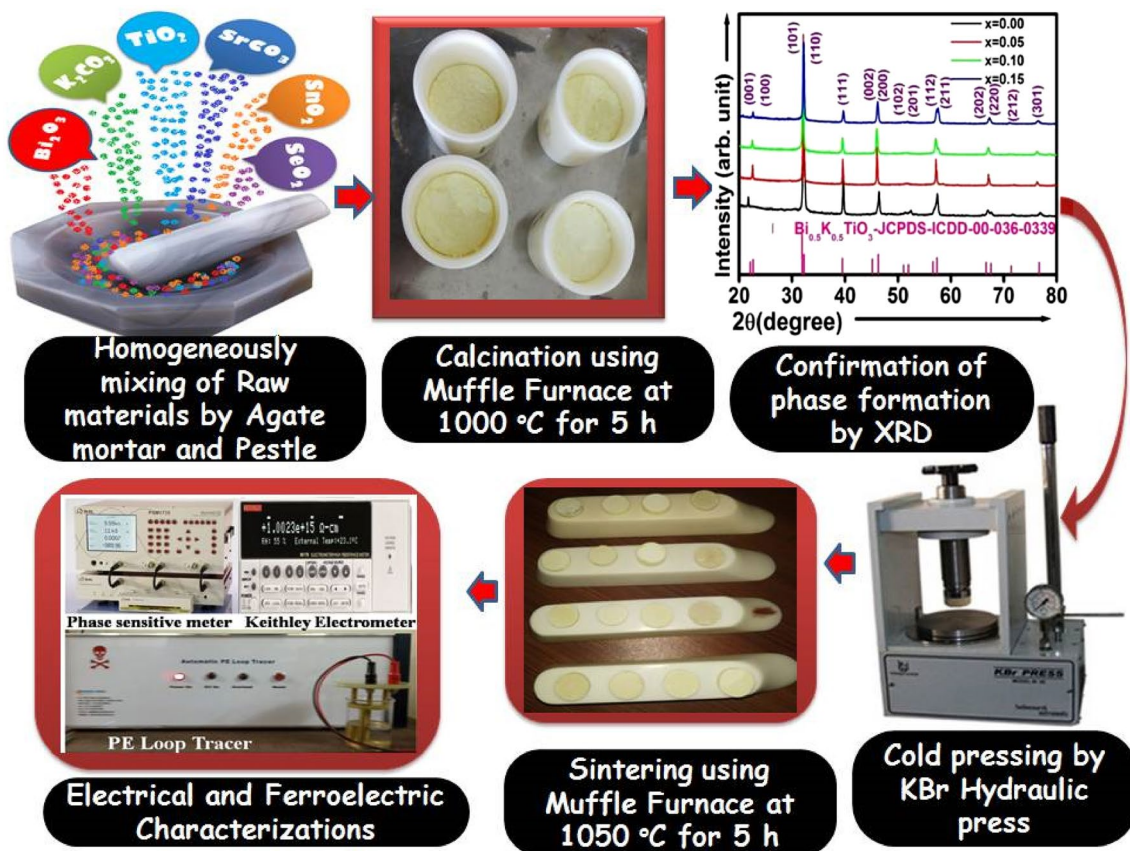


Fig. 1 Experimental configuration of solid-state reaction method and characterization

### 3 Results and discussions

#### 3.1 Structural analysis

The room temperature X-ray diffraction spectrum of the calcined powders of the synthesized material BKT-SSn-SSe at different compositions is given in Fig. 2. The XRD spectrum displayed the formation of the pure perovskite structure of the compound without any impurity phase or/and individual phases of the oxides and carbonates used as the ingredients for the material. The characteristic peaks of the prepared materials ranging from 20 to 80° (on a 2θ scale) are completely different from those of the constituent ones indicating the development of new perovskite samples. The polycrystalline nature of the prepared materials was described from the analysis of the diffraction peak intensity and from the pattern of the XRD. The materials crystallize in the tetragonal symmetry of bismuth potassium titanate (Bi<sub>0.5</sub>K<sub>0.5</sub>TiO<sub>3</sub>), and all the peaks were indexed by using the X'Pert High-score software (reference code ICDD-00-036-0339).

The obtained lattice parameters along with crystal data are given as  $a = b = 3.9180 \text{ \AA}$  and  $c = 4.0130 \text{ \AA}$ ,  $\alpha = \beta = \gamma = 90^\circ$ ,  $Z = 1$  with density =  $5.93 \text{ g/cm}^{-3}$  and cell

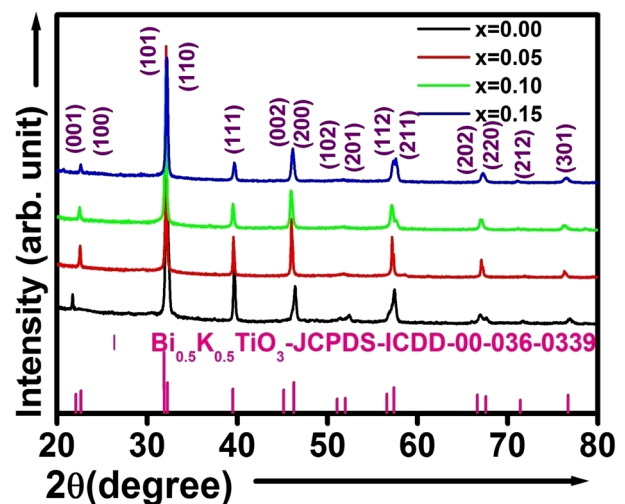


Fig. 2 Room temperature XRD spectrum of (1-2x) BKT + x Sn + x SSe ceramics at various concentrations

volume =  $61.60 \text{ \AA}^3$ . It is found that with the increase in the amount of the substituted materials (i.e., Sn-SSe) in BKT, the peaks of the XRD pattern move toward the left (the lower

value of  $2\theta$ ) because of the greater ionic radius of the substituted materials than that of pure BKT compound.

For detailed structural analysis of the prepared materials, the Rietveld refinement method was carried out, utilizing Maud software using the CIF file (CIF: NIMS\_MatNavi\_4295517175\_1\_2) of  $(\text{Bi}_{0.5}\text{K}_{0.5})\text{TiO}_3$  compound with tetragonal crystal system (space group, P4mm). In Fig. 3, the black solid symbols are the experimentally observed data/pattern, the red line symbolizes the Rietveld refinement simulation, and the green solid symbol represents the corresponding Bragg's position of the diffraction peaks. The refinement quality (validity), which is shown by a blue solid line in the plots, is determined by the difference between observed data and calculated data.

The reliability parameters ( $R$ -values) such as  $R_{\text{wp}}$ ,  $R_{\text{b}}$ ,  $R_{\text{exp}}$ , and the goodness of fit ( $\sigma$ ) are commonly used to represent the quality (accuracy) of the Rietveld refinement and the obtained cell parameters are tabulated in Table 1. The values of the cell parameters/ lattice constants of the prepared material (SSn-SSe modified BKT) show comparatively smaller

values than that of the previous work i.e.,  $\text{BaSnO}_3$ – $\text{BaSeO}_3$  (BSn-BSe) modified BKT ceramics [17]. This is because of the fact that the ionic radius of the substituted cations and the lattice parameter increases almost linearly with the ionic radius of the substituted cations [18]. The ionic radius of  $\text{Ba}^{2+}$  (1.35 Å) is higher than the ionic radius of  $\text{Sr}^{2+}$  (1.18 Å) [19]. The crystallite size ( $D$ ) and strain ( $\epsilon$ ) of the samples are calculated by using the Williamson–Hall equation [20] given by,

$$\beta \cos \theta = 4\epsilon \sin \theta + \frac{k\lambda}{D} \quad (1)$$

Here  $\beta$  indicates the FWHM,  $\theta$  is the Bragg diffraction angle of the considered peak,  $\lambda$  represents the wavelength of  $\text{CuK}\alpha$  radiation = 1.5406 Å, and  $k$  is the dimensionless form factor with a constant value of 0.89 for the tetragonal unit cell.

In Fig. 4, the slope and the intercept of the graph determine the strain and crystallize size of the compounds,

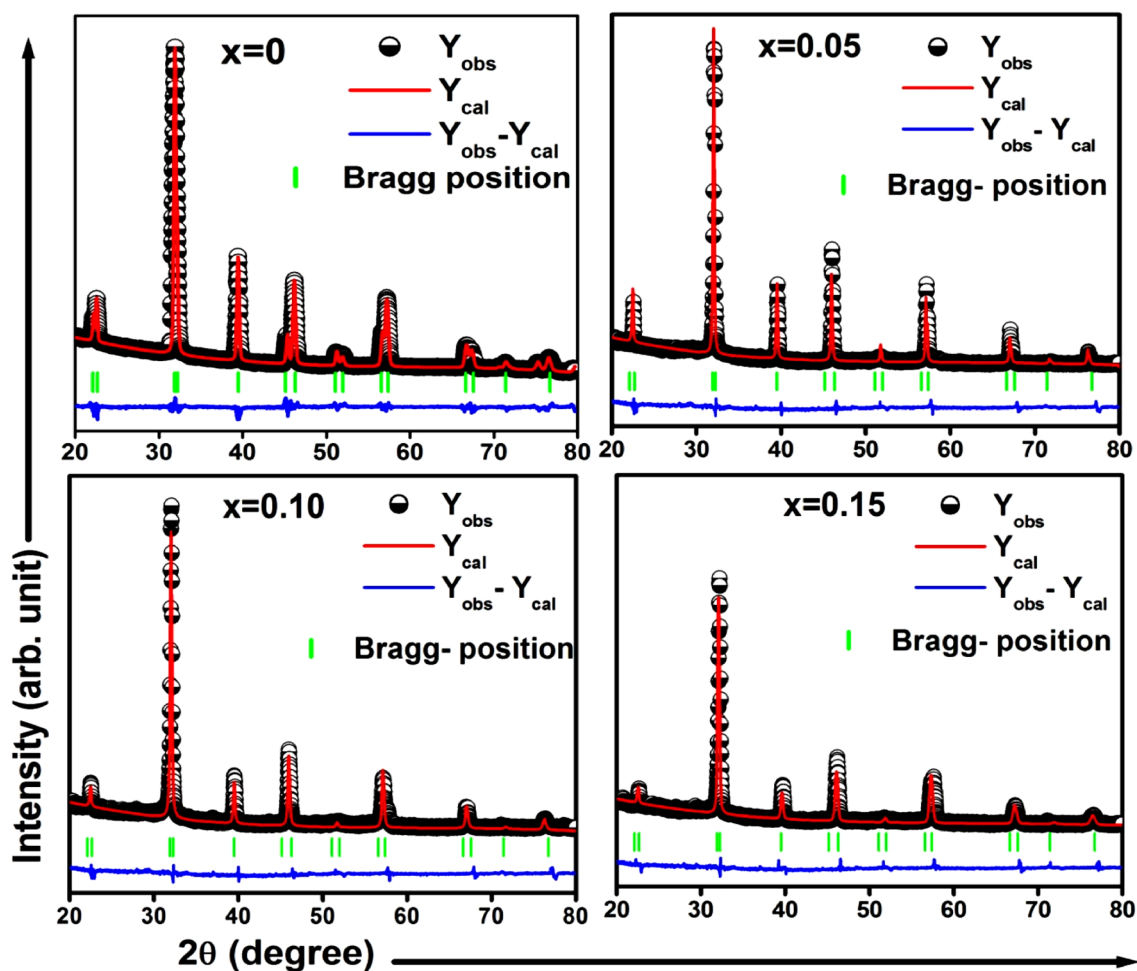
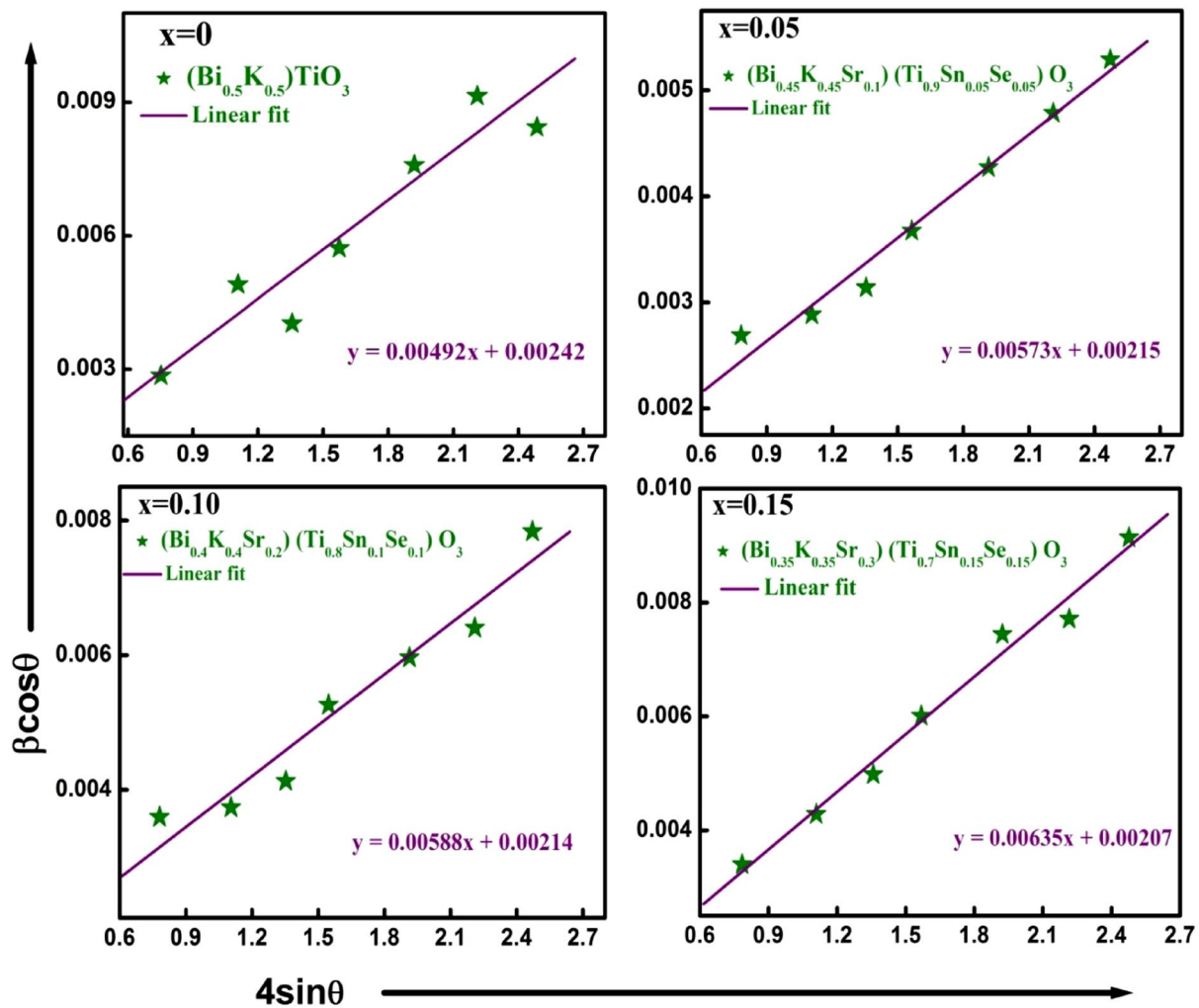


Fig. 3 Rietveld Refinement  $(1-2x)\text{BKT} + x\text{SSn} + x\text{SSe}$  ceramics at various concentrations

**Table 1** Unit cell dimension, reliability parameters, and crystallite size of (1-2x) BKT + x SSn + x SSe ceramics at various concentrations

Composition (x)	Crystal structure and space group	Lattice parameters (Å)		Reliability parameters (%)				Crystallite Size(D) and lattice strain ( $\epsilon$ )	
		a	c	R <sub>wp</sub>	R <sub>b</sub>	R <sub>exp</sub>	gof	D (nm)	$\epsilon$
0	Tetragonal and P4mm	3.930	3.918	10.17	10.83	9.33	1.09	56	0.0049
0.05		3.934	3.943	12.87	9.62	9.79	1.31	63	0.0057
0.10		3.945	3.954	14.62	9.69	9.70	1.50	64	0.0058
0.15		3.947	3.963	14.95	10.14	9.81	1.52	66	0.0063

**Fig. 4** Williamson–Hall plot of (1-2x) BKT + x SSn + x SSe ceramics at various concentrations

respectively. The values of crystallite size and strain of the studied materials are given in Table 1. The crystallite size of the compounds increases with the increase in the

substitution percentage as the ionic radius of the substituted materials is higher than at of the parent compounds.

### 3.2 Dielectric characteristics

The dielectric investigations specify the dielectric properties of a material as a function of frequency and temperature. The dielectric characteristics of ferroelectric materials mainly depend upon two components such as (i) dielectric constant ( $\epsilon_r$ ), and (ii) loss tangent ( $\tan \delta$ ). These two factors are very significant and decide the application potential of the dielectric materials. They are strongly dependent on the structure, chemical composition, defects that exist in the compound, and the experimental conditions (i.e., frequency, temperature, etc.) The dielectric constant determines the charge-holding capacity of the sample, and on the other hand,  $\tan \delta$  is defined as the ratio of energy loss to the energy stored in a capacitor. The dielectric characteristics examine the two fundamental electrical properties of the compounds, such as (i) the capacitive insulating nature (which signifies the electrical charge-storing capacity of the material), and (ii) the conduction nature (which signifies the ability of the material to transfer electric charge). In this work, the frequency and temperature variation of dielectric constant ( $\epsilon_r$ ) and dielectric loss ( $\tan \delta$ ) are investigated. Dielectric properties of solid materials can be well explained as a function of the frequency of applied electric field, temperature, crystal structure, and other parameters. The dielectric constant of a material is represented by,

$$\epsilon_r = \epsilon_r' - j\epsilon_r'' \tag{2}$$

Here  $\epsilon_r'$  and  $\epsilon_r''$  are the real and imaginary components of the dielectric constant, signifying the amount of energy stored in a dielectric material as polarization and energy loss, respectively [21]. The frequency-dependent real part of the dielectric constant ( $\epsilon_r'$ ) can be calculated by using the relation,

$$\epsilon_r' = \frac{C_p t}{\epsilon_0 A} \tag{3}$$

Here  $C_p$  represents the capacitance of the specimen in Farad (F),  $t$  is the thickness of the pellet,  $\epsilon_0$  represents the permittivity of free space and  $A$  stands for the area of the flat surface of the sintered pellet. Similarly, the complex or imaginary components of the dielectric constant ( $\epsilon_r''$ ) can be obtained by the equation,

$$\epsilon_r'' = \epsilon_r' \tan \delta, \text{ and} \tag{4}$$

$$\delta = 90^\circ - \theta \tag{5}$$

where  $\tan \delta$  is the dielectric loss which is proportional to the loss of energy from the applied field into the sample (this energy is dissipated as heat) and therefore denoted as dielectric loss and  $\theta$  is the phase angle.

**Fig. 5** Effect of frequency on dielectric constant at various temperatures (25 °C–500 °C) of (1-2x) BKT + x SSn + x SSe ceramics at various concentrations

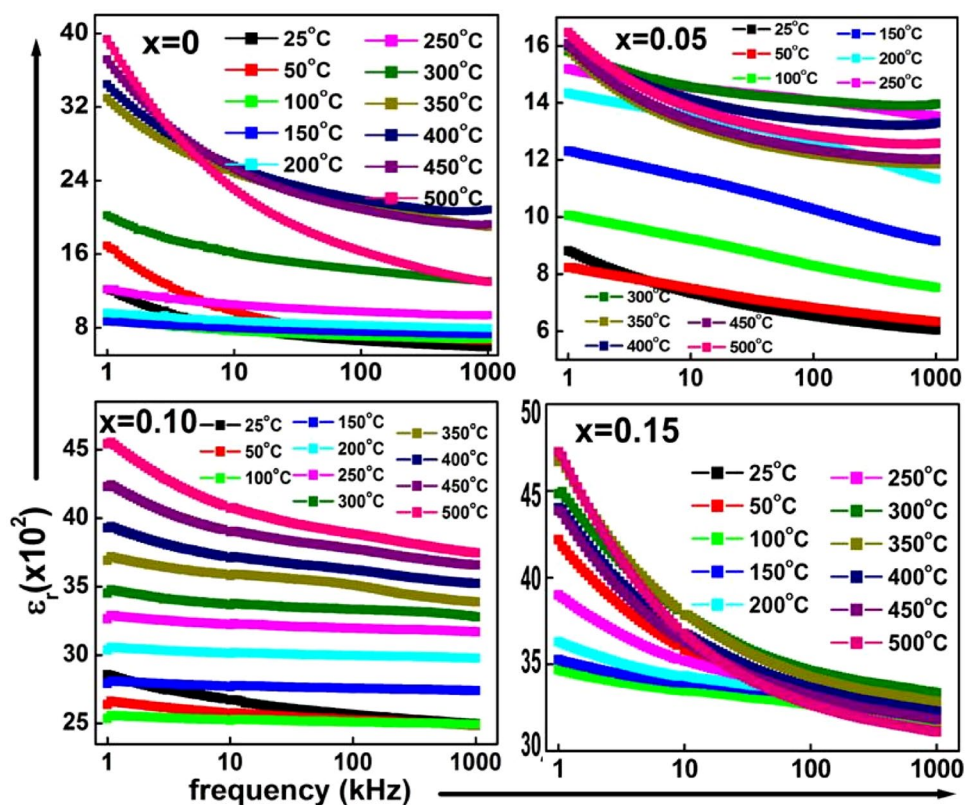
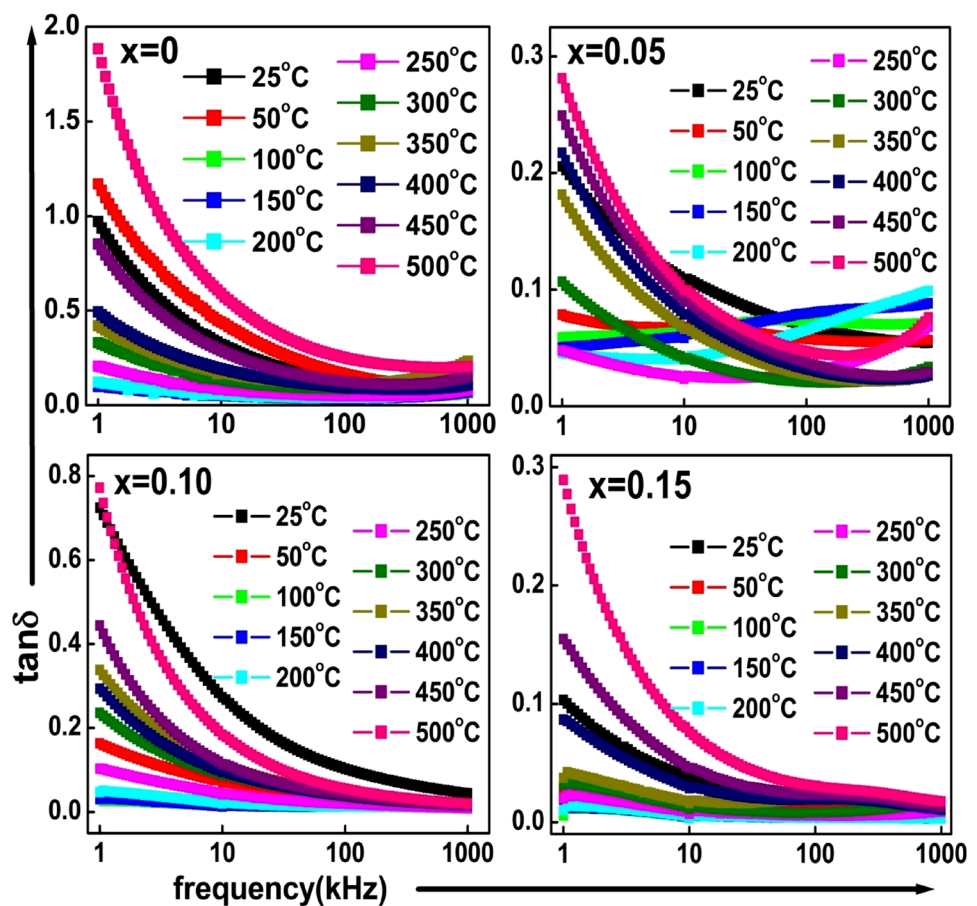


**Fig. 6** Effect of frequency on loss tangent at various temperatures (25 °C–500 °C) of (1-2x) BKT + x SSn + x SSe ceramics at various concentrations



### 3.2.1 Frequency variation of dielectric characteristics

Figures 5, 6 show the frequency variation of relative permittivity/ dielectric constant as well as tangent loss of the studied compound (BKT-SSn-SSe) for varying amounts of additives (such as 0, 5%, 10%, and 15%) in BKT over a broad temperature (25 °C–500 °C) and frequency (1 kHz–1 MHz) ranges.

The relative permittivity shows high values in low-frequencies sites and starts to decrease with an increase in frequency. The decrease in dielectric constant is rapid at low frequencies and becomes slow at higher frequencies, approaching towards the frequency-independent behavior. This type of trend suggests the existence of dielectric dispersion in low-frequency sites and it confirms the ferroelectric as well as dielectric characteristics of the materials [22]. In composites, in lower frequencies, the high value of  $\epsilon_r$ , corresponds to the heterogeneous conduction [23], but in some cases, the polaron hopping may cause low-frequency dispersion. The dispersion is rapid at lower frequencies but it is slow and approaches almost frequency-independent behavior at high frequencies (microwave frequency).

In the low-frequency site, different kinds of polarization processes are observed such as deformational (electronic

and ionic), and relaxation (orientational and interfacial) polarization. The net polarization of the dielectric ceramics is defined as the sum of all four kinds of polarizations [24]. First, electronic polarization arises because of the displacement of valence electrons with respect to the positive nucleus and this polarization appears at frequencies up to  $10^{16}$  Hz. Second, the ionic polarization is obtained owing to the displacement of positive and negative ions with respect to each other and this polarization occurs up to  $10^{13}$  Hz. Third, the dipolar polarization found in the sample has molecules with permanent electric dipole moments capable of changing orientation into the direction of the applied electric field and the maximum frequency for this polarization is  $10^{10}$  Hz. Finally, the space charge polarization appears as a result of the impedance of mobile charge carriers by interfaces, and such type of polarization typically takes place in the frequency range of 1– $10^3$  Hz. Ionic polarization plays a significant role in total polarization. Orientational polarization takes more time than electronic and ionic polarization hence decreases with frequency rise [25]. Therefore,  $\epsilon_r$  shows the maximum value at the low-frequency sites and then decreases as some polarizations diminish with an increase in frequency, and after a certain frequency limit except electronic polarization, all polarization processes vanish entirely. The dispersion

dielectric graph could be specified by the Maxwell–Wagner theory of Koop’s bi-layer model [26, 27]. This signifies that the dielectric material consists of two inhomogeneous layers such as the good conducting grains as well as the poor conducting grain boundaries. The charge carriers/ electrons are more active at grains and grain boundaries in the higher and lower-frequency sites, respectively. More energy is essential for the movement of the charge carriers in the low frequency. Since the grain boundaries offer high resistance, the charge carriers gather at the grain boundary and create a large amount of space charge polarization, resulting in a high value of the dielectric constant in this region of low frequency. In the high-frequency range, the energy required to move the charge carriers is less because the grains offer low resistance, hence dielectric constant is also low in the regions of high frequency [28]. It is also found that the value of the dielectric constant rises with an increase in temperature suggesting the interaction between electron and phonon [29]. In electron-lattice interaction, the energy exchange between electrons and lattice is because of the adsorption and radiation of phonons and is called the electron–phonon interaction. Moreover, the considerable increase in dielectric constant at high temperatures is observed at the lower frequency of 1 kHz, which is caused by the increased electrical conductivity [30]

Dielectric loss ( $\tan \delta$ ) is represented as dissipated energy in a dielectric system. It is considered to be caused by domain wall resonance. According to Eq. (4)  $\tan \delta$  is proportional to the imaginary part of the dielectric constant. In Fig. 6, the values of dielectric loss decline with a rise in frequency proposing that it varies inversely with frequency and this is the common property of dielectric compounds. The reduction in  $\tan \delta$  with frequency can be attributed to the fact that, at low frequencies, the value of  $\tan \delta$  is because of the movement of ions in the material. At moderate frequencies,  $\tan \delta$  is owing to the contribution of ion jumps, conduction loss of ion migration as well as ion polarization losses. Whereas for higher frequencies, ion vibration acts as the only source of loss tangent and therefore  $\tan \delta$  has the minimum value in this region [31].

The high values of  $\tan \delta$  in the lower frequency region are also because of the higher resistance of the grain boundary as the electrons in the grain boundaries are more active at low- frequencies, and similarly, the reverse situation is observed in the higher frequency site where the electrons in the grains are more active and the lower values of grain resistance produce low  $\tan \delta$ . On the other hand, the decrease in loss tangent with frequency rise may explain the dipole relaxation phenomenon [32]. With the addition of SSnSSe to BKT, the value of dielectric loss first reduces for  $x=0.05$  and then rises for other higher concentrations (i.e., for  $x=0.10$ , and  $0.15$ ).

**Table 2** Comparison of the maximum values of dielectric parameters ( $\epsilon_r$  and  $\tan \delta$ ) among the BKT-based materials with different compositions at 1 kHz

Compounds	Compositions						Ref				
	Dielectric constant ( $\epsilon_r$ )										
	x=0	x=0.05	x=0.1	x=0.15	x=0.2	x=0.2					
(1-x) (Bi <sub>0.5</sub> K <sub>0.50</sub> )TiO <sub>3-x</sub> (SrSnO <sub>3</sub> )-x (SrSeO <sub>3</sub> )	3432	1658	4533	4975	1410	1820	0.285	0.783	0.293	[33]	
(1-x) (Bi <sub>0.5</sub> K <sub>0.5</sub> ) TiO <sub>3-x</sub> Bi(Ni <sub>0.5</sub> Ti <sub>0.5</sub> )O <sub>3</sub>	1130	1680	1710	1670	1519	0.035	0.039	0.036	0.039	0.042	[34]
(1-x) Bi <sub>1/2</sub> K <sub>1/2</sub> TiO <sub>3-x</sub> Bi(Ni <sub>1/2</sub> Ti <sub>1/2</sub> )O <sub>3</sub>	1208	1252	1763	1564	1519	0.0459	0.0498	0.0697	0.0599	0.0567	[35]
Bi <sub>0.5(1-x)</sub> Pr <sub>x</sub> K <sub>0.5</sub> TiO <sub>3</sub>	520.1	713.87				0.10	0.1391				
(1-x) Bi <sub>0.5</sub> K <sub>0.5</sub> TiO <sub>3-x</sub> BaNb <sub>2</sub> O <sub>6</sub>	<b>x=0</b>	<b>x=0.005</b>	<b>x=0.01</b>	<b>x=0.02</b>	<b>x=0.03</b>	<b>x=0</b>	<b>x=0.005</b>	<b>x=0.01</b>	<b>x=0.02</b>	<b>x=0.03</b>	[8]
	2639	2847	3020	2618	2312	0.10	0.75	0.65	0.60	0.14	
0.82 Na <sub>0.5</sub> Bi <sub>0.5</sub> TiO <sub>3-0.18</sub> K <sub>0.5</sub> Bi <sub>0.5</sub> TiO <sub>3</sub>	893					0.037					[36]
0.82 Bi <sub>0.5</sub> Na <sub>0.5</sub> TiO <sub>3-0.18</sub> Bi <sub>0.5</sub> K <sub>0.5</sub> TiO <sub>3</sub> ceramics with 0–0.1 wt.% Nd <sub>2</sub> O <sub>3</sub>	925										[37]

The bold signifies the corresponding article’s reference number, proving the numerical value



The maximum values of the dielectric constant at 1 kHz are found to be 3432, 1658, 4533, and 4975 for  $x=0, 0.05, 0.10, 0.15$ , respectively. Similarly, the tangent loss values are observed to be 1.820, 0.285, 0.783, and 0.293 for  $x=0, 0.05, 0.10, 0.15$ , respectively. Table 2 listed the maximum values of dielectric constant and loss tangent of the BKT-based compounds at various compositions at 1 kHz. This table confirms that the present material shows the maximum value of the dielectric constant in comparison to others and this is one of the advantages of the prepared materials over others.

### 3.2.2 Temperature dependence of dielectric characteristics

The effect of temperature on relative permittivity along with loss tangent of the synthesized materials for different compositions at some selected frequencies (1 kHz–1 MHz) is given in Figs. 7 and 8, respectively. In Fig. 7, it is observed that the values of  $\epsilon_r$  remain constant up to particular values of frequency for all temperature, and with a further rise in temperature the values of  $\epsilon_r$  increase and become maximum at a particular temperature and then decreases with temperature rise. In this graph, a broad dielectric peak is observed between 360 and 420 °C. This peak suggests the phase transition from ferroelectric to paraelectric phase and is called the transition temperature ( $T_c$ ). In this graph, with increases in substitution percentage, the dielectric peak becomes more and more diffused

and disappears gradually. Here for  $x=0.15$ , the dielectric peak is absent. The observed peak (i.e., the  $T_c$  values) at different frequencies slightly changes and shifts towards a higher value of temperature with an increase in frequency. This frequency dispersion of  $T_c$  indicates that BKT ceramics are typical relaxor-structure ferroelectrics [7, 38]. The relaxor behavior in BKT ceramics confirms the positional disorder between  $K^+$  and  $Bi^{3+}$  cations on a 12-fold coordinated site. The dielectric loss also exhibited a similar feature in the studied temperature region associated with frequency-dependent maximum temperature [30]. A typical relaxor ferroelectric exhibit the following features [39]: (1) the ferroelectric to paraelectric phase transition extends over a broad temperature region (diffuse phase transition) in contrast with the sharp phase transition frequently observed in normal ferroelectrics; (2) no macroscopic structural change is observed during this transition; (3) the temperature of the maximum dielectric constant ( $T_{max}$ ) shifts toward a higher temperature, while its value decreases as the measuring frequency is increased over several orders of magnitude within the radio frequency (100 Hz–100 kHz); and (4) the dielectric loss shows the reversed trend (i.e., shifts towards the lower temperature with increase in frequency). In Fig. 8,  $\tan \delta$  varies in similar ways as that dielectric constant and the peak is observed at the same place as that of  $\epsilon_r$ . It is observed that the  $\tan \delta$  value rises sharply at high temperatures, and the

**Fig. 7** Effect of temperature on dielectric constant at various frequencies (1 kHz–1 MHz) of  $(1-2x)$  BKT +  $x$  SSn +  $x$  SSE ceramics at various concentrations

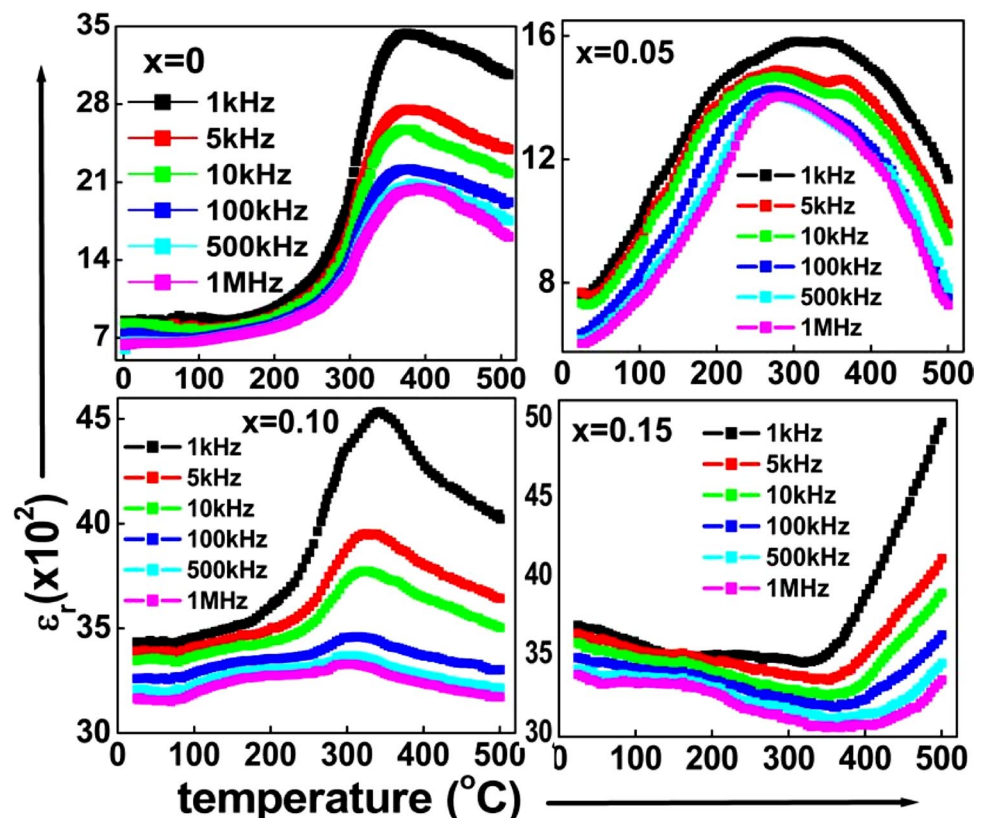
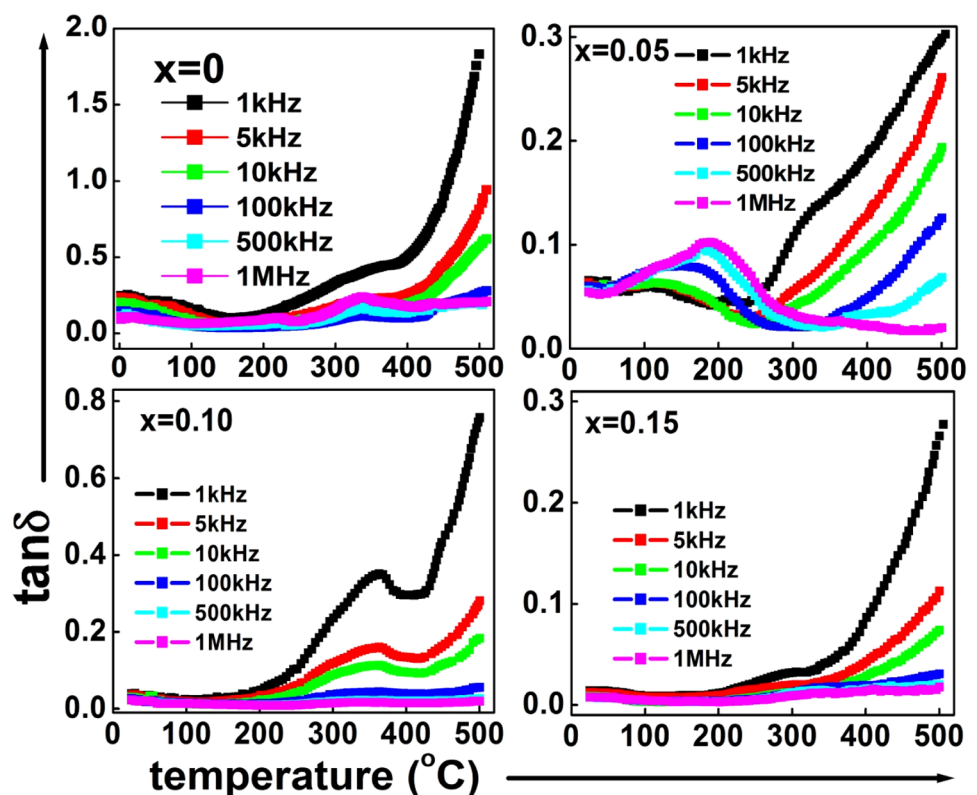


**Fig. 8** Effect of temperature on tangent loss at a selected frequency out of 1 kHz–1 MHz of  $(1-2x)$  BKT +  $x$  SSn +  $x$  SSe ceramics at various concentrations



increasing rate is slow at low temperatures. These types of the trend of tangent loss may be due to different reasons, such as high-temperature sintering causing defects like oxygen vacancy, scattering of thermally activated charge carriers, and the existence of the impurity phase [29]. At higher temperatures, the conductivity starts to dominate because of the presence of some unidentified defects in the material, which in turn, is likely for the rise in  $\tan \delta$ . The peak observed in the  $\tan \delta$  graph is known as the relaxation peak, which suggests the contribution of the grain boundary effect in the polarization process. This peak corresponds to the relation  $\omega\tau = 1$ , where  $\omega$  represents the angular frequency and  $\tau$  represents the Debye relaxation time. The peak in the  $\tan \delta$  graph, suggests the relaxation mechanism of the dipolar type, which shifts with the increase in frequency. But in the present study, the shifting of the peak is not prominent and a slight shifting is observed towards the lower temperature with an increase in frequency. From the above study, a high value of  $\epsilon_r$  and a low value of  $\tan \delta$  is observed, which makes the sample suitable for electronic devices, like transducers, capacitors, and microwave applications. According to thermodynamics, pressure, temperature, and volume are the three important thermodynamic parameters and the other variables are defined as the function of these quantities. In this work, the dielectric and conductivity parameters are explained as a function of temperature. Moreover, the

pressure varies in the reverse ways as that of temperature. With the increase in pressure, the height of the maximum value of the dielectric constant decreases and this shows the same effect as obtained by decreasing the temperature [40]. Similarly, the influence of free volume on the dielectric parameter is mainly observed in the case of polymer. The dielectric constant of a polymer is mainly influenced by two parameters. Such as (i) molecular polarizability and (ii) free volume. The dielectric constant remains almost constant with an increase in free volume size till the size reaches  $125 \text{ \AA}^3$  and thereafter it steeply increases [41].

### 3.3 Complex impedance spectroscopy

The complex impedance spectroscopy (CIS) technique is very popular because of the enormous potential for the characterization of different materials. It is widely used to characterize the electrical properties of materials and their interfaces with electronically conducting electrodes. This method demonstrates the separation among the grain, grain boundary, and electrode-interface effects. It provides information regarding the homogeneous and inhomogeneous distributions of these above effects and the porosity in the compounds. It investigates the microscopic properties of the samples such as charge diffusion, charge transfer, and dielectric relaxation, and distinguishes various polarization

mechanisms that exist in the materials. This CIS technique enables us to separate the resistive (real) and reactive (imaginary) components of the electrical parameters and hence provides a clear picture of the material properties. The complex formalism of the impedance is given by the relation:

$$Z^* = Z' - jZ'' = R_s - \frac{1}{j\omega C_s} \quad (6)$$

### 3.3.1 Frequency dependence of real impedance ( $Z'$ )

Figure 9 shows the frequency-dependent  $Z'$  and  $Z''$  (inserted) of the studied compounds BKT-SSn-SSe at different concentrations (i.e., 0, 5%, 10%, and 15%) within the experimental range of temperature (25 °C–500 °C). In low-frequency sites (below 100 kHz), the value of  $Z'$  decreases gradually for all compositions with the rise in frequency, and this suggests the increase of electrical conductivity in the compounds [42].

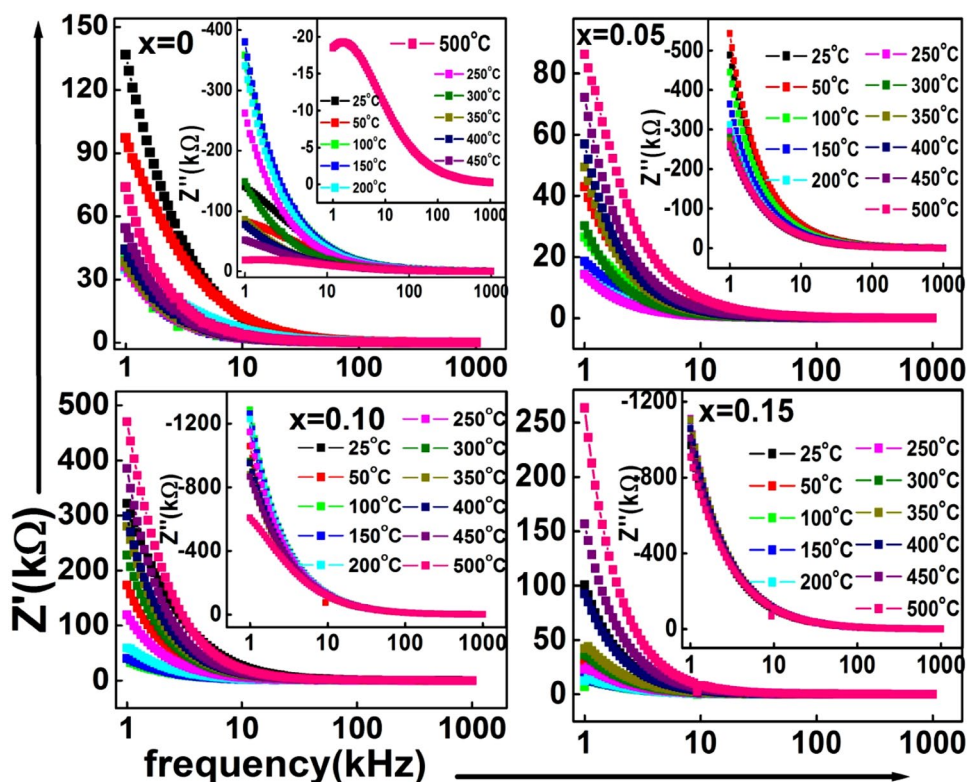
It is observed that  $Z'$  has higher values at lower frequencies and decreases monotonically with the rise in frequency and attains a constant value at the higher frequency part. Since  $Z'$  has strong frequency dependence in the lower regime then this could be attributed to the fact that the low-frequency region corresponds to high resistivity due to the effectiveness of the resistive grain boundaries in this region and shows the frequency independent behavior in the higher

frequency region [43]. On the other hand, in the higher-frequency range (> 100 kHz) the value of  $Z'$  merges to a constant value irrespective of frequency rising for all compositions and temperatures i.e., becomes frequency independent and this trend of  $Z'$  indicates the release of space charges due to the dropping in barrier property of the material [44]. The reduction in barrier properties of these materials with temperature rise may be a responsible factor for the enhancement of the ac conductivity of the materials at higher frequencies. At high frequencies, the space charge has lesser time to relax and the recombination would be faster. Hence, the space charge polarization is reduced at higher frequencies leading to a merge of curves at higher frequencies [45]. Here the value of  $Z'$  first decreases from 25 to 100 °C for all compositions, suggesting the NTCR behavior of the compounds, and for other higher temperatures (150 °C–500 °C) the values of  $Z'$  rises with the increase in temperature signifying the PTCR behavior of the studied compounds.

### 3.3.2 Frequency dependence of imaginary impedance ( $Z''$ )

Figure 9 (inserted) signifies the loss spectrum (frequency dependence of  $Z''$ ) of the studied material. It is found that, in the low-frequency region, the values of  $Z''$  decreases monotonically with an increase in temperature, and after a certain value of frequency (100 kHz for  $x=0$ , 0.05 and 10 kHz for  $x=0.10$ , 0.15), they combine to a fixed value. This nature of the graph signifies the presence of space

**Fig. 9** Effect of frequency on  $Z'$  and  $Z''$  at various temperatures out of 25–500 °C of (1-2x) BKT + x SSn + x SSe ceramics at various concentrations



charge polarization in low-frequency sites and temperature-dependent dielectric relaxation at high temperatures [46]. In the present work, except for  $x=0$ , no peak is observed in the loss spectrum for all compositions, which suggests the lack of dissipation of current in the experimental range of temperature and frequency. For  $x=0$  compositions, a peak in the  $Z''$  vs frequency is observed at 500 °C confirming the existence of the electrical relaxation mechanism in the compounds [47]. As the relaxation peak has the tendency to appear at a lower frequency and higher temperature, the occurrences of the peak may be beyond the experimental range, i.e., lower than 1 kHz and higher than 500 °C. The frequency at which  $Z''$  attains the maximum value is called the relaxation frequency ( $f_r$ ) and the inverse of  $f_r$  is known as the relaxation time of the sample. Generally, in dielectric materials, the relaxation species may be because of the presence of immobile species/electrons at low temperatures and defects/vacancies at higher temperatures [48].

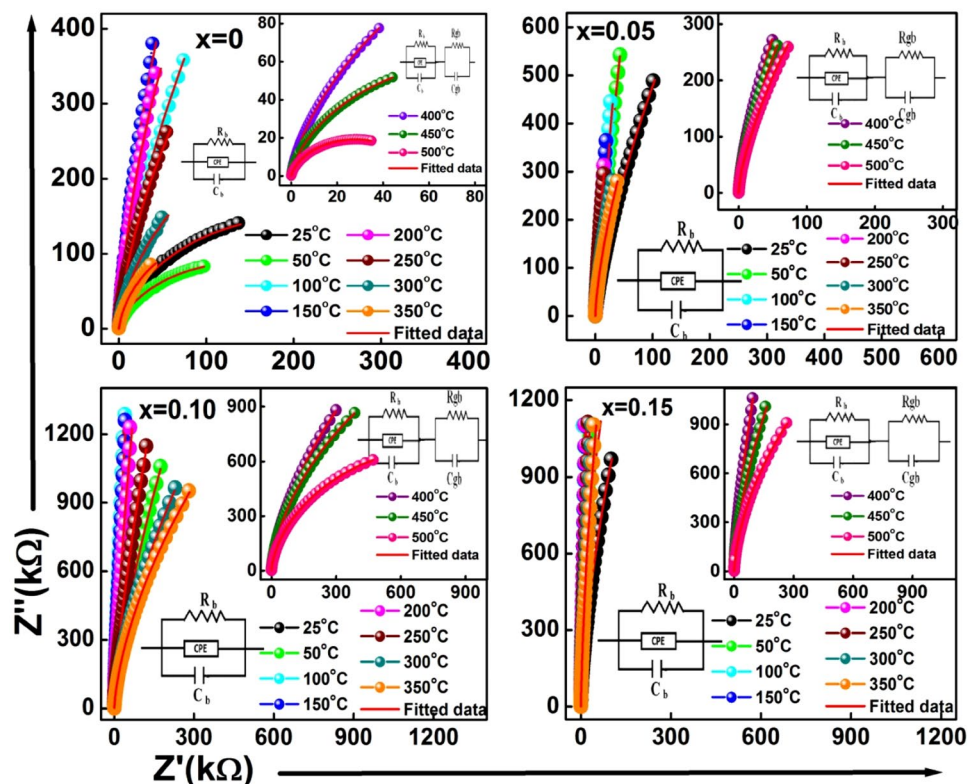
### 3.3.3 Nyquist plots

Figure 10 represents the Nyquist plots (variation of the imaginary component ( $Z''$ ) with the real component ( $Z'$ ) of complex impedance) within the temperature range of 25 °C–500 °C of the studied material for all compositions. These graphs compare the experimentally observed results

with the theoretical fitting data using the commercial software ZSIMPWIN of version 2.

The impedance spectroscopy of the samples is studied with the development of complex semicircles whose pattern varies with temperature. In this figure, for all compositions of the materials, from 25 to 350 °C the impedance curves are fitted by a single semicircle and for the other higher temperature (400 °C–500 °C) the impedance curves are fitted by two semicircles. The single semicircle in this graph represents the grain effect and is modeled by the equivalent circuit of RQC, where R and C are connected in parallel with Q (constant phase element/ CPE) in between them. In such a case, the capacitance represents space charge polarization and resistance represents the conductive path. The double semicircle in this electrical process, representing both the grain and grain boundary effect of the compound, can be modeled in terms of the equivalent electrical circuit according to the ‘‘Brick layer model’’ [49]. In this work, from temperature, 400 °C–500 °C for all compositions, the impedance data are represented using two semicircular arcs, comprising the series combination of the RQC-RC circuit. There is an excellent match established between the experimental result and the theoretical fitted data. The resistance and capacitance along with CPE of grain (i.e.,  $R_g$ ,  $C_g$ , and Q) and grain boundary (i.e.,  $R_{gb}$ , and  $C_{gb}$ ) are given in Table 3. The semicircular behavior can be explained by considering the following mathematical equation:

**Fig. 10** Nyquist plots of  $(1-2x)$  BKT +  $x$  SSn +  $x$  SSe ceramics at various concentrations with some selected temperatures (25–500 °C)



**Table 3** Resistance, CPE ( $Q$ ), and capacitance of grain and grain boundary of (1-2x) BKT + x SSn + x SSe ceramics at various concentrations with some selected temperatures (25 °C to 500 °C)

Composition	Temp.(°C)	Model	R <sub>b</sub> (Ω)	CPE	C <sub>b</sub> (F)	R <sub>gb</sub> (Ω)	C <sub>gb</sub> (F)
x = 0	25	(RQC)	4.48 × 10 <sup>05</sup>	1.10 × 10 <sup>-08</sup>	2.57 × 10 <sup>-10</sup>		
	50	(RQC)	4.22 × 10 <sup>05</sup>	3.88 × 10 <sup>-08</sup>	2.90 × 10 <sup>-10</sup>		
	100	(RQC)	4.03 × 10 <sup>05</sup>	1.46 × 10 <sup>-09</sup>	3.00 × 10 <sup>-10</sup>		
	150	(RQC)	1.74 × 10 <sup>06</sup>	3.38 × 10 <sup>-10</sup>	2.82 × 10 <sup>-10</sup>		
	200	(RQC)	2.71 × 10 <sup>06</sup>	5.44 × 10 <sup>-10</sup>	2.95 × 10 <sup>-11</sup>		
	250	(RQC)	3.20 × 10 <sup>06</sup>	9.75 × 10 <sup>-10</sup>	3.88 × 10 <sup>-10</sup>		
	300	(RQC)	3.66 × 10 <sup>06</sup>	1.63 × 10 <sup>-09</sup>	3.66 × 10 <sup>-10</sup>		
	350	(RQC)	3.84 × 10 <sup>06</sup>	2.91 × 10 <sup>-09</sup>	2.19 × 10 <sup>-10</sup>		
	400	(RQC)(RC)	5.01 × 10 <sup>06</sup>	2.54 × 10 <sup>-08</sup>	9.31 × 10 <sup>-10</sup>	1.27 × 10 <sup>01</sup>	2.84 × 10 <sup>-10</sup>
	450	(RQC)(RC)	5.34 × 10 <sup>06</sup>	4.53 × 10 <sup>-08</sup>	8.71 × 10 <sup>-10</sup>	1.99 × 10 <sup>01</sup>	4.11 × 10 <sup>-10</sup>
x = 0.05	500	(RQC)(RC)	5.97 × 10 <sup>06</sup>	4.40 × 10 <sup>-08</sup>	5.46 × 10 <sup>-10</sup>	2.82 × 10 <sup>01</sup>	9.86 × 10 <sup>-10</sup>
	25	(RQC)	7.80 × 10 <sup>06</sup>	9.33 × 10 <sup>-10</sup>	1.87 × 10 <sup>-10</sup>		
	50	(RQC)	6.08 × 10 <sup>06</sup>	3.35 × 10 <sup>-10</sup>	1.54 × 10 <sup>-10</sup>		
	100	(RQC)	5.23 × 10 <sup>06</sup>	5.26 × 10 <sup>-10</sup>	1.26 × 10 <sup>-10</sup>		
	150	(RQC)	7.08 × 10 <sup>06</sup>	6.52 × 10 <sup>-10</sup>	9.90 × 10 <sup>-10</sup>		
	200	(RQC)	8.18 × 10 <sup>06</sup>	7.02 × 10 <sup>-10</sup>	1.01 × 10 <sup>-10</sup>		
	250	(RQC)	1.23 × 10 <sup>07</sup>	6.26 × 10 <sup>-10</sup>	9.83 × 10 <sup>-10</sup>		
	300	(RQC)	6.43 × 10 <sup>07</sup>	1.03 × 10 <sup>-09</sup>	4.77 × 10 <sup>-10</sup>		
	350	(RQC)	9.62 × 10 <sup>07</sup>	3.16 × 10 <sup>-09</sup>	4.71 × 10 <sup>-10</sup>		
	400	(RQC)(RC)	4.03 × 10 <sup>08</sup>	2.61 × 10 <sup>-08</sup>	1.69 × 10 <sup>-09</sup>	2.29 × 10 <sup>06</sup>	6.12 × 10 <sup>-10</sup>
x = 0.10	450	(RQC)(RC)	6.74 × 10 <sup>08</sup>	3.00 × 10 <sup>-08</sup>	1.29 × 10 <sup>-09</sup>	2.46 × 10 <sup>06</sup>	6.82 × 10 <sup>-10</sup>
	500	(RQC)(RC)	9.41 × 10 <sup>08</sup>	4.98 × 10 <sup>-09</sup>	5.25 × 10 <sup>-10</sup>	3.41 × 10 <sup>06</sup>	6.91 × 10 <sup>-10</sup>
	25	(RQC)	2.69 × 10 <sup>06</sup>	9.97 × 10 <sup>-09</sup>	1.12 × 10 <sup>-10</sup>		
	50	(RQC)	2.23 × 10 <sup>06</sup>	5.60 × 10 <sup>-10</sup>	1.11 × 10 <sup>-10</sup>		
	100	(RQC)	1.46 × 10 <sup>06</sup>	1.26 × 10 <sup>-10</sup>	1.67 × 10 <sup>-10</sup>		
	150	(RQC)	7.56 × 10 <sup>07</sup>	3.72 × 10 <sup>-11</sup>	1.08 × 10 <sup>-10</sup>		
	200	(RQC)	8.19 × 10 <sup>07</sup>	1.23 × 10 <sup>-10</sup>	1.17 × 10 <sup>-10</sup>		
	250	(RQC)	1.22 × 10 <sup>08</sup>	6.32 × 10 <sup>-10</sup>	1.18 × 10 <sup>-10</sup>		
	300	(RQC)	1.52 × 10 <sup>08</sup>	1.36 × 10 <sup>-09</sup>	1.18 × 10 <sup>-10</sup>		
	350	(RQC)	7.42 × 10 <sup>08</sup>	1.21 × 10 <sup>-09</sup>	1.15 × 10 <sup>-10</sup>		
x = 0.15	400	(RQC)(RC)	7.85 × 10 <sup>08</sup>	2.03 × 10 <sup>-09</sup>	1.17 × 10 <sup>-10</sup>	1.09 × 10 <sup>06</sup>	5.12 × 10 <sup>-09</sup>
	450	(RQC)(RC)	7.13 × 10 <sup>08</sup>	4.40 × 10 <sup>-09</sup>	2.15 × 10 <sup>-10</sup>	2.44 × 10 <sup>06</sup>	2.40 × 10 <sup>-10</sup>
	500	(RQC)(RC)	8.00 × 10 <sup>08</sup>	5.49 × 10 <sup>-09</sup>	1.57 × 10 <sup>-10</sup>	3.99 × 10 <sup>06</sup>	3.83 × 10 <sup>-10</sup>
	25	(RQC)	1.99 × 10 <sup>07</sup>	1.89 × 10 <sup>-10</sup>	1.36 × 10 <sup>-10</sup>		
	50	(RQC)	1.68 × 10 <sup>07</sup>	5.72 × 10 <sup>-11</sup>	1.36 × 10 <sup>-10</sup>		
	100	(RQC)	1.39 × 10 <sup>07</sup>	1.50 × 10 <sup>-11</sup>	1.00 × 10 <sup>-15</sup>		
	150	(RQC)	1.65 × 10 <sup>08</sup>	2.25 × 10 <sup>-11</sup>	1.40 × 10 <sup>-10</sup>		
	200	(RQC)	1.68 × 10 <sup>08</sup>	2.48 × 10 <sup>-11</sup>	1.39 × 10 <sup>-10</sup>		
	250	(RQC)	2.61 × 10 <sup>08</sup>	2.89 × 10 <sup>-11</sup>	1.36 × 10 <sup>-10</sup>		
	300	(RQC)	4.12 × 10 <sup>08</sup>	1.43 × 10 <sup>-11</sup>	1.34 × 10 <sup>-10</sup>		
x = 0.15	350	(RQC)	5.08 × 10 <sup>08</sup>	1.60 × 10 <sup>-10</sup>	7.20 × 10 <sup>-10</sup>		
	400	(RQC)(RC)	9.80 × 10 <sup>08</sup>	5.27 × 10 <sup>-09</sup>	5.36 × 10 <sup>-10</sup>	2.10 × 10 <sup>07</sup>	1.56 × 10 <sup>-10</sup>
	450	(RQC)(RC)	1.00 × 10 <sup>09</sup>	1.93 × 10 <sup>-10</sup>	1.28 × 10 <sup>-10</sup>	2.95 × 10 <sup>04</sup>	3.58 × 10 <sup>-10</sup>
	500	(RQC)(RC)	2.50 × 10 <sup>09</sup>	5.13 × 10 <sup>-09</sup>	3.91 × 10 <sup>-10</sup>	4.04 × 10 <sup>06</sup>	1.89 × 10 <sup>-10</sup>

$$\left(Z''^2 - \frac{R}{2}\right)^2 + Z''^2 = \frac{R^2}{4} \quad (7)$$

where  $Z'$  and  $Z''$  are the real and imaginary parts of impedance, respectively, and  $R$  is the resistance of the material

[42]. The observed semicircular arcs have their centers below the real  $Z$ -axis signifying the existence of a non-Debye type relaxation mechanism in the compounds [50]. For the ideal Debye model, the centre of the semicircular arc is present on the real  $Z$ -axis. The CPE, in the equivalent

circuit elements also confirms the deviation from the ideal Debye-type model in the prepared materials. The propagation of the electrical signal through a resistive/ capacitive branched transmission line can be well described by the differential equation which describes the diffusion process of charge carriers. It was noted that a branched transmission line exhibits constant phase behavior [51] and hence is an electrical equivalent of a constant phase element (CPE). The CPE impedance is defined as

$$Z_{CPE} = Z_0(j\omega)^{-\alpha} \tag{8}$$

where both  $Z_0$  and  $\alpha$  are frequency-independent and temperature-dependent real parameters. The parameter  $Z_0$  determines the magnitude of dispersion and the value of  $\alpha$  lies between 0 and 1 (i.e.  $0 \leq \alpha \leq 1$ ). For a purely resistive circuit,  $\alpha = 0$ , whereas for a purely capacitive circuit  $\alpha = 1$  [51, 52]. As suggested by Scheider [53], branch transmission lines produce a constant phase angle, hence, termed as a constant phase element. This type of behavior is usually observed

at the electrode–electrolyte interface of the polycrystalline ceramic disc samples.

For better investigation of the non-Debye type relaxation process, the depressed semicircles are drawn at 350 °C for all compounds as shown in Fig. 11. The different value of the depression angles 11.62°, 4.14°, 7.11°, and 2.76° are observed for  $x = 0, 0.05, 0.10,$  and  $0.15$ , respectively, confirming the non-Debye type of relaxation mechanism in the compounds in the experimental range of temperature and frequency.

### 3.4 Conductivity analysis

In dielectric material, the motion of the charge carriers gives rise to the conduction current and polarizes the dielectric. The electrical conductivity of the sample provides information regarding the nature and motion of the charge carriers and the domain structure and depends on the nature of the dielectric substance. There is a strong correlation between the frequency and temperature response of the electrical

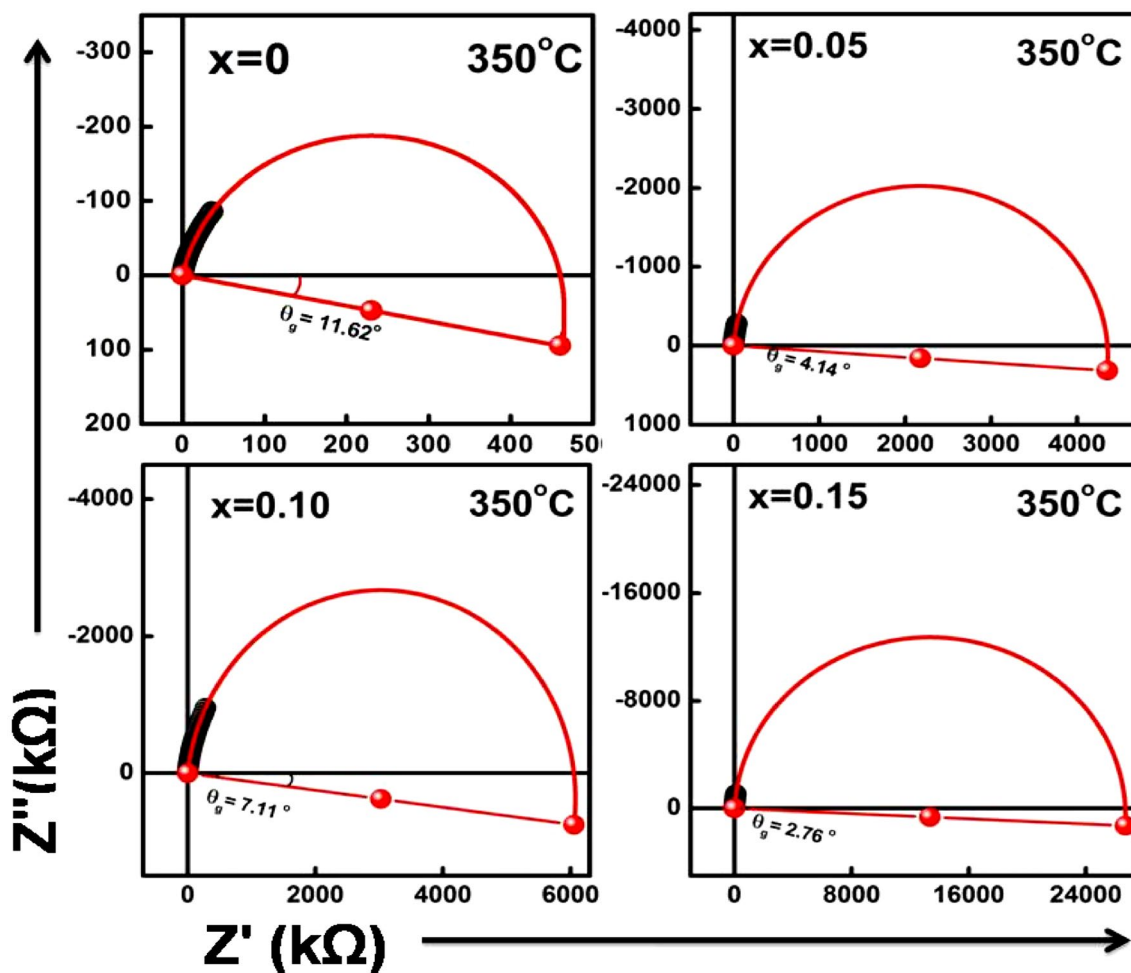


Fig. 11 Depressed semicircles of  $(1-2x)\text{BKT} + x\text{SSn} + x\text{SSe}$  ceramics at various concentrations at 350 °C with depression angle

conductivity of the compounds. The temperature dependence of  $\sigma_{ac}$  shows the existence of a single or multiple relaxation processes present in the compounds. In solid materials, two kinds of conduction processes are found such as (i) localized transport oxygen vacancy; (ii) long-range ac conductivity. In the case of polar compounds, the conduction process may be electronic or/ and ionic. Based upon the temperature and purity of the compound, the proportion of ionic to the electrical conductivity of the compound varies.

### 3.4.1 Frequency dependence of conductivity analysis

The frequency variation of ac-conductivity for the samples BKT-SSn-SSE, with  $x=0, 0.05, 0.10, 0.15$  at constant temperatures (25 °C–500 °C) are plotted in Fig. 12. Using the dielectric parameters (dielectric constant along with tangent loss), the ac conductivity ( $\sigma_{ac}$ ) of the material is calculated through the following relation [54],

$$\sigma_{ac} = \omega \epsilon_r \epsilon_0 \tan \delta \quad (9)$$

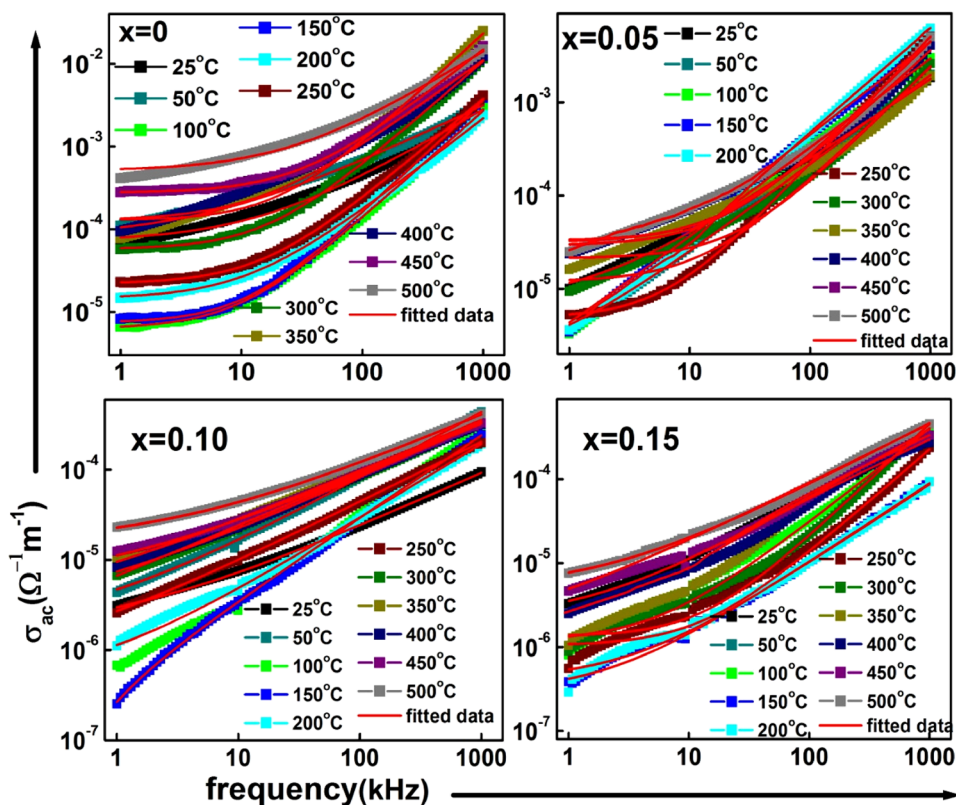
where  $\omega = 2\pi f$  is the angular frequency,  $\epsilon_r$  is the relative permittivity,  $\epsilon_0$  is the permittivity of free space and  $\tan \delta$  is the loss tangent, which is defined as  $\tan \delta = \epsilon_r''/\epsilon_r'$  (where  $\epsilon_r''$ ,  $\epsilon_r'$  are imaginary and real part of relative permittivity respectively).

There is a sharp rise in ac conductivity is observed with a frequency rise in the low- temperature site. But with the temperature rise, the increasing rate of conductivity becomes slower. For high temperatures and lower frequency sites, a plateau-like pattern is observed for all compositions except  $x=0.05$  provides the frequency-independent part or dc conductivity which may be due to thermally assisted space charge carriers. The plateau region extends to higher frequencies with the increase in temperature. It is to be noted that, at low frequencies, the random diffusion of charge carriers via hopping gives rise to a frequency-independent conductivity [55]. Alternatively, at a higher frequency and lower temperature, the frequency dispersion part represents the ac conductivity. The frequency variation of  $\sigma_{ac}$  of the materials is explained by using Jonscher's universal power law [56],

$$\sigma_{ac} = \sigma_{dc} + A\omega^n \quad (10)$$

Here the ac conductivity curves are fitted non-linearly and obey the above law. According to Jonscher, the source of frequency-dependent ac conductivity lies in the relaxation phenomenon because of the mobile charge carriers. When the hopping of charge carriers takes place from their original site to another new site, they remain in the state of motion between the two minima of the potential energy. Here A stands for a constant, depends on temperature, and defines the polarizability strength, similarly,

**Fig. 12** Effect of frequency on ac conductivity of (1-2x) BKT+x SSn+x SSE ceramics at various concentrations with different temperatures



$n$  represents the temperature-dependent exponent with the value  $0 < n < 1$ .  $A$  has the units of conductivity and  $n$  is dimensionless. According to many body interaction models [57], the interaction between all dipoles participating in the polarization process is characterized by the parameter  $n$ . For  $n = 0$ , the conduction mechanism is pure Debye type, while  $n < 1$  represents the deviation from the Debye model i.e., represents the non-Debye type conduction process that exists in the compound. The values of

$A$ , along with  $n$  of the prepared compound at different temperatures, obtained from the fitting results for all concentrations are listed in Table 4. The experimental data of ac conductivity shows good agreement with the theoretical value fitted using power law. From the table, the value of  $n < 1$  proposes the non-Debye type of conduction exists in the compounds [58]. The rise of ac conductivity ( $\sigma_{ac}$ ) with a rise in frequency and temperature is determined by the cation disordering between the existing space charges

**Table 4** Values of  $A$  and  $n$  of  $(1-2x)$  BKT +  $x$  SSn +  $x$  SSe ceramics at various concentrations

Temp (°C)	Compositions (x)							
	x=0		x=0.05		x=0.10		x=0.15	
	A	n	A	n	A	n	A	n
25	$2.03 \times 10^{-08}$	0.855	$1.20 \times 10^{-08}$	0.861	$2.28 \times 10^{-08}$	0.957	$4.91 \times 10^{-09}$	0.816
50	$1.99 \times 10^{-07}$	0.797	$3.68 \times 10^{-09}$	0.954	$1.20 \times 10^{-09}$	0.874	$3.30 \times 10^{-11}$	0.833
100	$4.18 \times 10^{-11}$	0.901	$5.44 \times 10^{-09}$	0.955	$8.48 \times 10^{-10}$	0.920	$1.92 \times 10^{-10}$	0.969
150	$2.35 \times 10^{-11}$	0.863	$5.02 \times 10^{-09}$	0.991	$8.01 \times 10^{-10}$	0.912	$2.01 \times 10^{-10}$	0.941
200	$3.76 \times 10^{-10}$	0.926	$1.39 \times 10^{-09}$	0.911	$2.26 \times 10^{-09}$	0.821	$1.97 \times 10^{-10}$	0.845
250	$1.69 \times 10^{-10}$	0.824	$4.91 \times 10^{-11}$	0.811	$1.96 \times 10^{-08}$	0.669	$2.85 \times 10^{-12}$	0.924
300	$2.55 \times 10^{-10}$	0.870	$1.05 \times 10^{-10}$	0.953	$7.33 \times 10^{-08}$	0.608	$3.59 \times 10^{-12}$	0.935
350	$2.28 \times 10^{-10}$	0.833	$4.39 \times 10^{-11}$	0.907	$1.40 \times 10^{-07}$	0.566	$4.98 \times 10^{-09}$	0.640
400	$4.77 \times 10^{-09}$	0.960	$2.93 \times 10^{-10}$	0.897	$1.31 \times 10^{-07}$	0.565	$2.72 \times 10^{-09}$	0.674
450	$1.67 \times 10^{-09}$	0.856	$1.42 \times 10^{-10}$	0.827	$1.09 \times 10^{-07}$	0.879	$2.68 \times 10^{-08}$	0.705
500	$5.05 \times 10^{-08}$	0.905	$1.37 \times 10^{-10}$	0.851	$1.42 \times 10^{-07}$	0.871	$1.66 \times 10^{-08}$	0.740

**Fig. 13** Effect of the inverse of absolute temperature on ac conductivity at different frequency of  $(1-2x)$  BKT +  $x$  SSn +  $x$  SSe ceramics at various concentrations

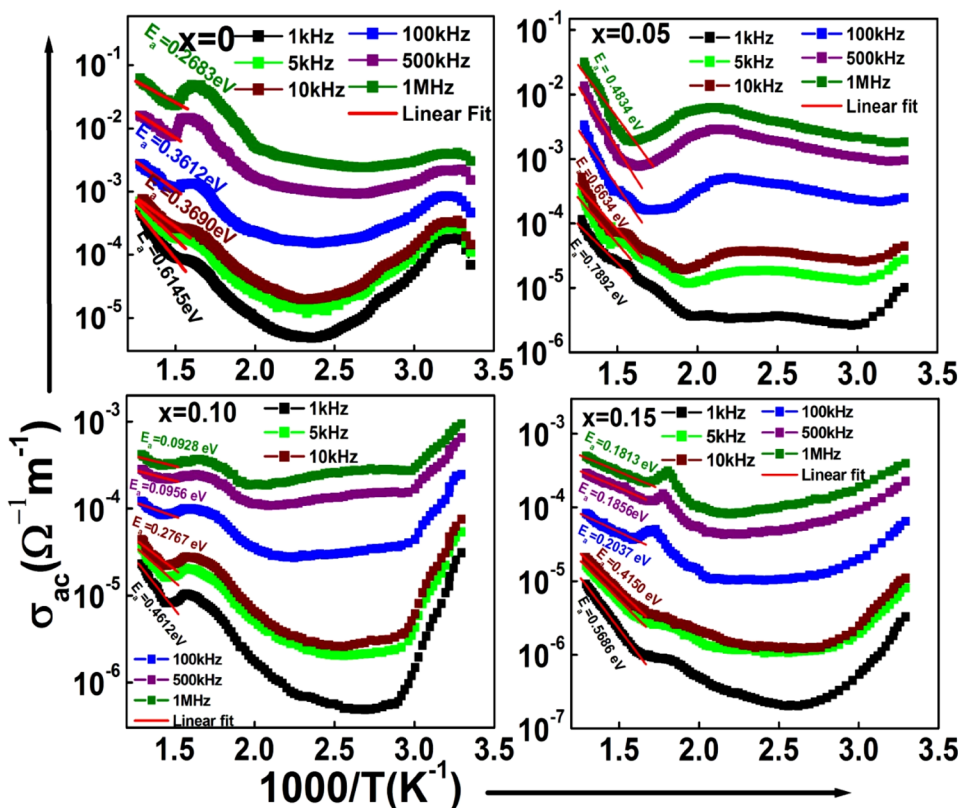




**Table 5** Comparison of activation energy (in eV) of (1-2x) BKT + x SSn + x SSe ceramics at various concentrations with different frequencies

Frequency (kHz)	Activation energy (E <sub>a</sub> ) (eV)							
	Composition (x) and Error (ζ)							
	x=0	ζ	x=0.05	ζ	x=0.10	ζ	x=0.15	ζ
1	0.614	0.061	0.789	0.013	0.461	0.011	0.568	0.056
5	0.474	0.011	0.719	0.012	0.324	0.020	0.433	0.043
10	0.369	0.012	0.663	0.008	0.276	0.015	0.415	0.041
50	0.361	0.019	0.572	0.035	0.127	0.019	0.203	0.020
500	0.315	0.003	0.552	0.059	0.095	0.031	0.185	0.018
1000	0.268	0.010	0.483	0.007	0.092	0.020	0.181	0.025

and the surroundings and this is the general feature of  $\omega^n$ . Thermodynamically, the influence of pressure on the maximum conductivity is equivalent to that of dielectric constant [59] i.e., with the increase in pressure, the maximum value of conductivity decreases.

### 3.4.2 Temperature dependence of conductivity analysis

Figure 13 shows the variation of ac-conductivity ( $\sigma_{ac}$ ) of the prepared compounds at different compositions, with the inverse absolute temperature ( $1000/T$ ) at various frequencies (1 kHz–1 MHz). The values of ac conductivity change very slowly in low-temperature sites and very quickly in high-temperature sites. This plot indicates that for all frequencies, the values of ac conductivity increase with temperature rise and this may be because of the existence of space charges in the compounds, and the cation disordering between the charge carriers and the neighboring sites [60].

The activation energy ( $E_a$ ) of the studied sample depending on the thermally activated process is evaluated using the Arrhenius equation [61],

$$\sigma = \sigma_0 \exp\left(\frac{-E_a}{K_B T}\right) \quad (11)$$

where  $\sigma_0$  stands for the pre-exponential factor and  $K_B$  represents the Boltzmann constant. The equation is valid for the excitation of free electrons from the Fermi level to the highest density of states. The values of  $E_a$  are evaluated from the slopes of the linear fitting lines in the higher-frequency site and tabulated in Table 5. With the increase in frequency, the value of activation energy decreases for all compositions. The different values of  $E_a$  propose the occurrence of different conduction mechanisms in the compounds. The calculated value of  $E_a$  is the summation of the activation energies of the charge carriers and the free energy of the carrier hopping. With the enhancement of frequency, the probability of hopping of the charge carriers increases, and this reduces the values of the activation energy with an increase of frequency. At the higher temperature region, all the curves

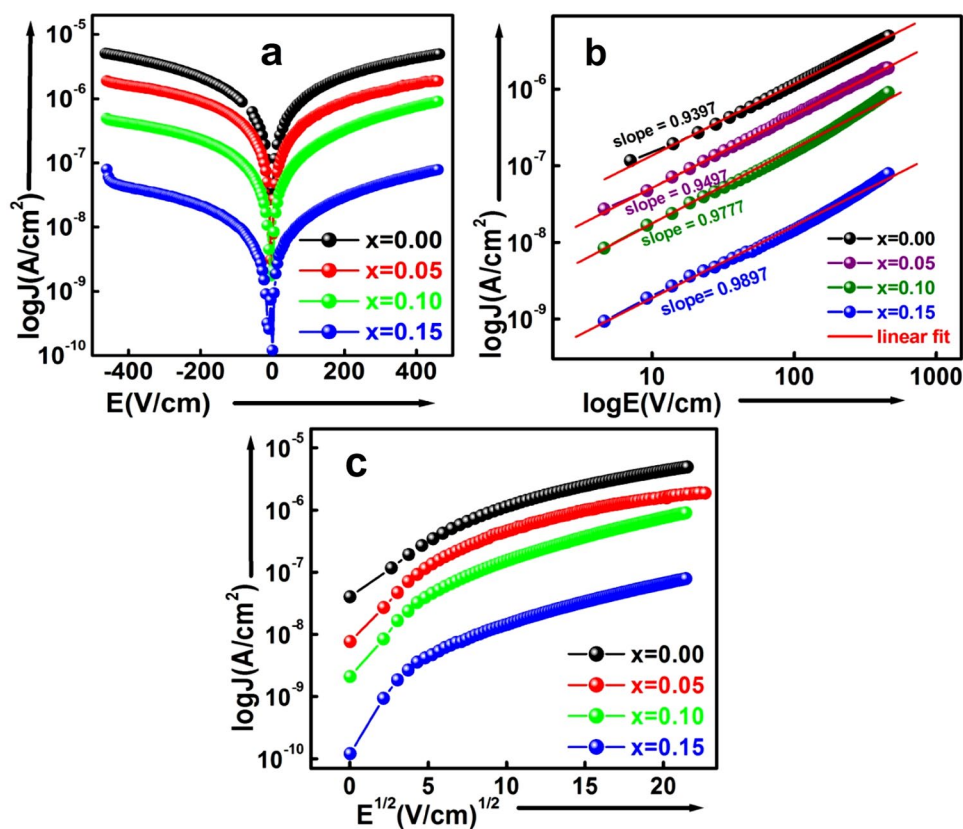
of different frequencies seem to merge, and dispersion in conductivity narrows down with temperature rise. It suggests that the space charges are released and recombined at higher temperatures. The value of the activation energy obtained at high temperatures is attributed to the thermal motion of the oxygen vacancies or the development of the relationship between the oxygen vacancies and residual cations in the grain boundary [62, 63]. The higher value of  $\sigma_{ac}$  in a higher temperature range shows the predominant role of ionic charge carriers, such as oxygen vacancies.

### 3.5 Leakage current characteristics

In the dielectric material, there are two conduction mechanisms are found such as (i) Electrode limited conduction mechanism and (ii) Bulk-limited conduction mechanism. The electrode-limited conduction mechanism, depending on the electrical properties at the electrode dielectric contact and also called the injection-limited conduction mechanism. The other conduction mechanism which depends only on the properties of the dielectric itself is called bulk-limited conduction mechanisms or transport-limited conduction mechanisms.

The electrode-limited conduction mechanisms include (1) Schottky or thermionic emission (2) Fowler–Nordheim tunneling, (3) direct tunneling, and (4) thermionic-field emission. The bulk-limited conduction mechanisms include (1) Poole–Frenkel emission, (2) hopping conduction, (3) Ohmic conduction, (4) space-charge-limited conduction, (5) ionic conduction, and (6) grain-boundary-limited conduction [64]. In the present work, some of the conduction mechanisms are discussed. The electric field ( $E$ ) dependence of current density ( $J$ ) (i.e., J-E characteristics) of the prepared compounds BKT-SSn-SSe for all concentrations at room temperature is displayed in Fig. 14a–c. Figure 14a depicts the current density vs. electric field of the studied compound in both the opposite polarities starting from -400 kV/cm to 400 kV/cm through the origin. The values of  $J$  increase smoothly up to 50 kV/cm for all compositions and after that, the increasing rate

**Fig. 14** Room temperature (a)  $\log J$  vs.  $E$  plot, (b)  $\log J$  vs.  $\log E$  plot, (c)  $\log J$  vs.  $E^{1/2}$  plot of  $(1-2x)$  BKT +  $x$  SSn +  $x$  SSe ceramics at various concentrations



gets reduced. This figure is symmetric on both sides of the origin, which suggests the various kinds of polarization mechanisms present in the materials such as Ohmic conduction, space charge-limited current conduction, Poole–Frenkel emission, ionic conduction, Schottky emission, etc. [64]. By the substitution of SSn–SSe in the parent BKT ceramic, the leakage current value successfully decreases. The values of current density are found to be  $8.643 \times 10^{-6}$  A/cm<sup>2</sup>,  $2.035 \times 10^{-6}$  A/cm<sup>2</sup>,  $5.756 \times 10^{-7}$  A/cm<sup>2</sup>, and  $9.120 \times 10^{-8}$  A/cm<sup>2</sup> for  $x=0, 0.05, 0.10, 0.15$ , respectively. Here the values of leakage current density ( $J$ ) are of the order of  $10^{-7}$  A/cm<sup>2</sup> suggesting the dielectric properties of the material [65]. The small values of  $J$  make the materials useful for the fabrication of possible electronic devices. Figure 14b signifies the room temperature;  $\log J$  vs.  $\log E$  plot for all compositions in the experimental range of temperature. Here the  $\log J$  curves are fitted linearly with the slope  $m \approx 1$  (displayed in Fig. 14b) in both the high- and low-electric field regions, which suggests that in the whole regions of the field, the charge transport mechanism is predominated by the Ohmic conduction. Ohmic conduction is caused by the movement of mobile electrons in the conduction band and holes in the valence band. The current density of Ohmic conduction can be expressed as,

$$j = \sigma E = nq\mu E \quad (12)$$

where  $\sigma$  represents the electrical conductivity,  $n$  is the number of electrons in the conduction band;  $\mu$  is electron mobility [66]. The Ohmic conduction current is due to the mobile electrons in the conduction band or holes in the valence band and it linearly dependent on the electric field. In some materials, at high electric field region, the values of the slope are found to be 2 and a steep rise of current density is observed due to the gathering of excess amount of space charges. Such a type of conduction mechanism is called space-charge-limited current conduction (SCLC). However, this conduction mechanism is absent in the studied material in this experimental range of electric field.

The graph between  $\log J$  and  $E^{1/2}$  called the Schottky emission (SE) plot for all compositions at room temperature is shown in Fig. 14c. In Schottky emission/thermionic emission, by acquiring sufficient energy through thermal activation, the electrons can overcome the energy barrier/Schottky barrier at the metal–dielectric interface and are capable to go to the dielectric. The Schottky emission is well explained by the relation,

$$J = A^* T^2 \exp \left[ \frac{-q \left( \varphi_B - \sqrt{qE/4\pi\epsilon_r\epsilon_0} \right)}{k_B T} \right], \text{ and} \quad (13)$$

$$A^* = \frac{4\pi q k^2 m^*}{h^3} = \frac{120 m^*}{m_0} \quad (14)$$

where  $A^*$  represents the effective Richardson constant,  $m_0$  is the free electron mass,  $m^*$  is the effective electron mass in the dielectric,  $h$  is the Planck's constant,  $E$  signifies the electric field across the material, and  $\varphi_B$  stands for the barrier height [64]. For dielectric films, particularly at a higher temperature one of the common conduction mechanisms frequently observed is the thermionic emission. To evaluate, the barrier height at the metal–dielectric interface, this plot is one of the best methods. During the Schottky emission (i.e. thermionic emission), the electrons in the electrode will be able to go to the dielectric material if they can obtain enough energy to overcome the Schottky barrier. The required energy is provided by thermal activation [67]. From Eq. (13), it is found that, if the conduction current is governed by Schottky emission,  $\log J$  varies linearly with  $E^{1/2}$  i.e., the  $\log J$  vs.  $E^{1/2}$  plot should be a straight line, but in this work, for all compositions the curves are not linear, suggesting the absence of SE is in the prepared compound.

### 3.6 Ferroelectric study

The room temperature, PE hysteresis loops of the studied material BKT-SSn-SSe at different compositions with frequencies 50 Hz and 8 kV/cm of the applied field are shown in Fig. 15. Due to the experimental limitation, we are unable to apply a sufficient amount of electric field to get saturated symmetric loops. However, the obtained loops signify the ferroelectric behaviors of the studied material. The silver-coated sintered pellets of different areas and thicknesses for various concentrations such as (1.031 cm<sup>2</sup> and 0.192 cm), (0.870 cm<sup>2</sup> and 0.217 cm), (0.859 cm<sup>2</sup> and 0.249 cm), and (0.875 cm<sup>2</sup> and 0.272 cm) for 0, 5%, 10%, and 15%, respectively, were taken for the measurements.

The obtained results of remnant polarization ( $2P_r$ ), as well as the coercive field ( $E_c$ ) of the compounds, are found to be (0.072  $\mu\text{C}/\text{cm}^2$  and 1.016 kV/cm), (0.192  $\mu\text{C}/\text{cm}^2$  and 1.145 kV/cm), (0.383  $\mu\text{C}/\text{cm}^2$  and 1.204 kV/cm), (0.519  $\mu\text{C}/\text{cm}^2$  and 1.358 kV/cm) for  $x=0, 0.05, 0.1, 0.15$ , respectively. It is observed that with the rise in substitution concentration the  $2P_r$  value of the parent compounds increases successfully. Hence the addition of SSn-SSe to BKT enhances the ferroelectric behavior.

**Fig. 15** Room temperature hysteresis loop of (1-2x) BKT + x SSn + x SSe ceramics at various concentrations with 50 Hz

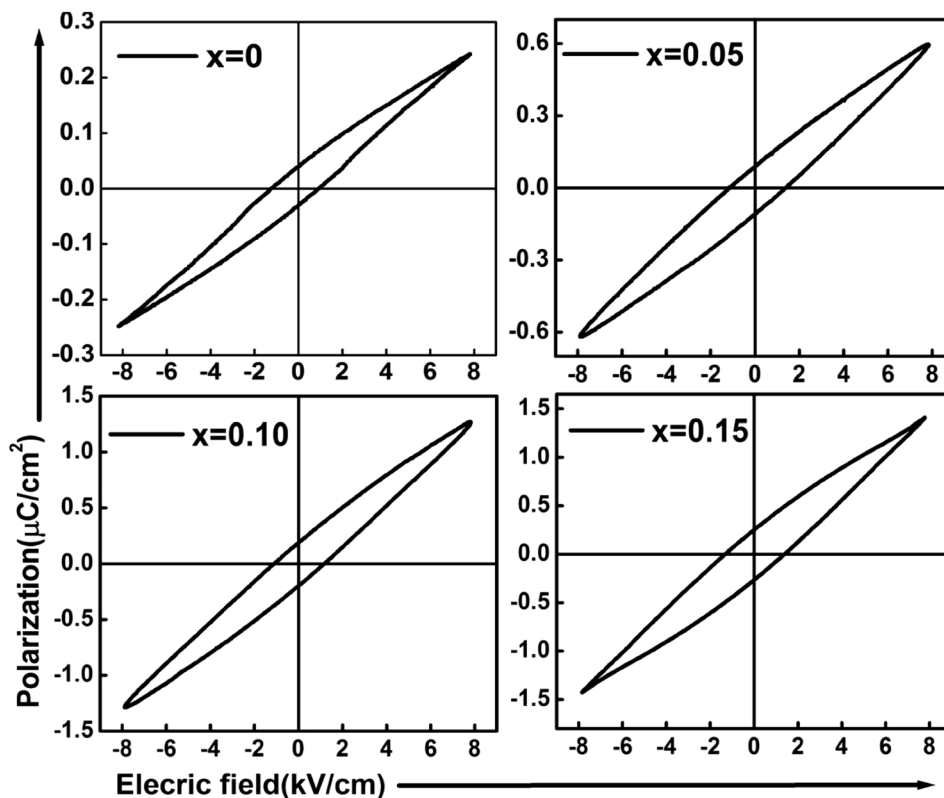


**Table 6** Comparison of the maximum values of dielectric parameters ( $\epsilon_r$  and  $\tan \delta$ ) between  $(1-2x)$  BKT +  $x$  SSn +  $x$  SSe and  $(1-2x)$  BKT +  $x$  SSn +  $x$  SSe ceramics at 1 kHz

Compositions (x)	BSn-BSe modified BKT		SSn-SSe modified BKT	
	$\epsilon_r$	$\tan \delta$	$\epsilon_r$	$\tan \delta$
	0	3432	1.82	3432
0.05	3837	0.79	1658	0.28
0.10	2342	0.92	4533	0.78
0.15	1604	1.21	4975	0.29

## 4 Conclusion

The polycrystalline ferroelectric ceramics  $(1-2x)$   $(\text{Bi}_{0.5}\text{K}_{0.5})\text{TiO}_3-x(\text{SrSnO}_3)-x(\text{SrSeO}_3)$  with  $x=0, 0.05, 0.10, 0.15$  have successfully been prepared through conventional solid-state reaction techniques. The room temperature XRD spectrum of the calcinated powder samples has been considered from  $20^\circ$  to  $80^\circ$  of the Bragg diffraction angle, suggesting the development of new perovskite single-phase compounds with no impurity phases. The studied material possesses a tetragonal unit cell along with the reliable values of cell constants obtained from Rietveld refinement. The cell constants of the prepared material are less than that of the previous work (BSn-BSe modified BKT) due to the smaller ionic radius of the  $\text{Sr}^{2+}$  ( $1.13 \text{ \AA}$ ) than that of  $\text{Ba}^{2+}$  ( $1.35 \text{ \AA}$ ). The average values of crystallite size of the materials evaluated from the  $W \sim H$  plot and found to be 56 nm, 63 nm, 64 nm, and 66 nm for  $x=0, 0.05, 0.10$ , and  $0.15$ , respectively [17]. The dielectric characteristics of the material suggest the polarization processes of the material are described by the Clausius–Mossotti relation. The peak at the  $T_c$  indicates the phase transition from ferroelectric to para-electric phase. The loss tangent of the material, explains the dipole relaxation phenomenon in the compound. The prepared sample shows higher values of dielectric constant and lower value of loss tangent as compared to BSn-BSe modified BKT [17] as shown in Table 6.

In the impedance spectroscopy, the compound shows both NTCR (at lower temperatures) and PTCR (at higher temperatures) behaviors, and the Nyquist plot proposes the non-Debye type relaxation mechanism present in the compound. The ac-conductivity of the material follows Joncher's universal power-law model and the activation energy at a higher temperature is calculated using the Arrhenius formula. The value of the ac-conductivity of the present sample is less than that of BSn-BSe modified BKT. This is due to the higher values of  $\tan \delta$  of BSn-BSe modified

BKT and it obeys Eq. (9). The JE characteristics of the compound show a very small amount of leakage current density (i.e., of the order of  $10^{-7} \text{ A/cm}^2$ ) at room temperature and determine the Ohmic conduction mechanism present in the compounds. The values of leakage current density of the sample are two orders less than that of BSn-BSe modified BKT. At  $x=0.15$  the value of  $J$  for the present material is found to be  $9.120 \times 10^{-08} \text{ A/cm}^2$  but for BSn-BSe modified BKT it is found to be  $1.012 \times 10^{-06}$ . The ferroelectric nature of the compound is confirmed by the room-temperature PE-hysteresis loops. With the substitution of SSn-SSe to the parent BKT, the  $2P_r$  values of the compound gradually increase.

**Data Availability Statement** The authors confirm that the data supporting the findings of this work are available within the article. Raw data that support the findings of the study are available from the corresponding author, upon reasonable request.

## References

1. A. Banerjee, S. Bose, Chem. Mater. **16**, 5610–5615 (2004)
2. B. Jaffe, W.R. Cook, H. Jaffe, *Piezoelectric ceramics* (Academic Press, London, 1971)
3. G. Shirane, K. Suzuki, J. Phys. Soc. Jpn. **7**, 333–333 (1952)
4. Y. Saito, H. Takao, T. Tani, T. Nonoyama, K. Takatori, T. Homma, T. Nagaya, M. Nakamura, Nat. Lond. **432**, 84–87 (2004)
5. M. Zhu, L. Hou, Y. Hou, J. Liu, H. Wang, H. Yan, Mater. Chem. Phys. **99**, 329–332 (2006)
6. P. Phetnoi, S. Niemcharoen, R. Muanghlua, M. Sutapun and N. Vittayakorn, ECTI-CON, (2010) 962–965.
7. Y. Hiruma, R. Aoyagi, H. Nagata, T. Takenaka, Jpn. J. Appl. Phys. **44**, 5040–5044 (2005)
8. Y. Pu, P. Gao, T. Wu, X. Liu, Z. Dong, J. Electron. Mater. **44**, 332–340 (2015)
9. E. Baba, D. Kan, Y. Yamada, M. Haruta, H. Kurata, Y. Kanemitsu, Y. Shimakawa, J. Phys. D. **48**, 455106 (2015)
10. M. Glerup, K.S. Knight, F.W. Poulsen, Mater. Res. Bull. **40**, 507–520 (2005)
11. M.A. Green, K. Prassides, P. Day, D.A. Neumann, Int. j. inorg. mater. **2**, 35–41 (2000)
12. L.T. Vlaev, M.M. Nikolova, G.G. Gospodinov, Monatshefte Chem. **136**, 1553–1566 (2005)
13. M.-L. Liang, Y.-X. Ma, C.-L. Hu, F. Kong, J.-G. Mao, Dalton Trans. **47**, 1513–1519 (2018)
14. M. Wildner, G. Giester, N. Jb, Miner. Abh **184**, 29–37 (2007)
15. Q. Chen, K. Su, Z. Zhao, Q. Ma, J. Non-Cryst. Solids **498**, 448–454 (2018)
16. A. Bachvarova-Nedelcheva, R. Iordanova, St. Yordanov, Y. Dimitriev, J. Non-Cryst. Solids **355** (2009) 2027–2030.
17. B.B. Arya, R.N.P. Choudhary, Solid State Sci. **109**, 106381 (2020)
18. Sk. Anirban, A. Dutta, Solid State Ion. **309** (2017) 137–145.
19. <http://abulafia.mt.ic.ac.uk/shannon/>
20. K.A. Aly, N.M. Khalil, Y. Algamal, Q.M. Saleem, J. Alloys Compd **676**, 606–612 (2016)
21. M.M. Hassan, A.S. Ahmed, M. Chaman, W. Khan, A.H. Naqvi, A. Azam, Mater Res. Bull. **47**, 3952–3958 (2012)
22. J.C. Anderson, *Dielectrics* (Chapman & Hall, London, 1964)
23. Y. Zhi, A. Chen, J. Appl. Phys. **91**, 5325–5333 (2002)
24. M Barsoum Fund. Ceram. Mc Graw Hill, New York (1977) p 543.

25. N. Shukla, V. Kumar, D.K. Dwivedi, J. Non Oxide Glasses **8**, 47–57 (2016)
26. E. Barsoukov, J.R. Macdonald, 2nd ed., Impedance Spectroscopy Theory, Experiment and Applications, vol. 14, Wiley-Interscience, New York, 2005
27. C.G. Koops, Phys. Rev. **83**, 121–124 (1951)
28. S. Shojaei, S.A. Hassanzadeh-Tabrizi, M. Ghashang, Ceram. Int. **40**, 9609–9613 (2014)
29. B.B. Arya, M. Mohanty, R.N.P. Choudhary, Mater. Chem. Phys. **279**, 12571 (2022)
30. J.F. Yang, Y.D. Hou, C. Wang, M.K. Zhu, H. Yan, Appl. Phys. Lett. **91**, 023118 (2007)
31. N.A. Hegab, A.E. Bekheet, M.A. Afifi, L.A. Wahaba, H.A. Shehata, J. Ovonic Res. **3**, 71 (2007)
32. S. Nath, S.K. Barik, R.N.P. Choudhary, J. Mater. Sci. Mater. Electron. **27**, 8717–8724 (2016)
33. P. Jarupoom, P. Jaita, R. Yimnirun, G. Rujijanagul, D.P. Cann, Curr. Appl. Phys. **15**, 1521–1528 (2015)
34. P. Jaita, P. Jarupoom, D.R. Sweatman, G. Rujijanagul, J. Asian Ceram. Soc. **9**, 947–963 (2021)
35. C.Y. Ng, K.A. Razak, J. Alloys Compd **509**, 942–947 (2011)
36. Z. Yang, B. Liu, L. Wei, Y. Hou, Mater. Res. Bull. **43**, 81–89 (2008)
37. Z. Yang, Y. Hou, B. Liu, L. Wei, Ceram. Int. **35**, 1423–1427 (2009)
38. M. Hagiwara, & S. Fujihara, Jpn J Appl Phys, 54 (1015) 10ND10
39. W.Z. Zhu, A. Kholkin, P.Q. Mantas, J.L. Baptista, Mater. Chem. Phys. **73**, 62–69 (2002)
40. A.H. Scott, Rubber Chem. Technol. **9**, 449–467 (1936)
41. R. Ramani, R. Ramachandran, G. Amarendra, S. Alam, J. Phys. Conf. Ser. **618**, 012025 (2015)
42. S. Brahma, R.N.P. Choudhary, S.A. Shivashankar, J. Phys. Chem. Solids **73**, 357–362 (2012)
43. S.A. Ansari, A. Nisar, B. Fatma, W. Khan, A.H. Naqvi, Mater Sci Eng B **177**, 428–435 (2012)
44. H. Jain, C.H. Hsieh, J. Non-Cryst. Solids **172**, 1408–1412 (1994)
45. S. Pattanayak, B.N. Parida, P.R. Das, R.N.P. Choudhary, Appl. Phys. A **112**, 387 (2013)
46. K. Lily, K. Kumari, R.N.P. Choudhary, K. Prasad, J. Alloys Compd. **453**, 325–331 (2008)
47. S. Chatterjee, P.K. Mahapatra, R.N.P. Choudhary, A.K. Thakur, Phys. Stat. Sol. **201**, 588–595 (2004)
48. A.K. Jonscher, The ‘universal’ dielectric response. Nature **267**, 673 (1977)
49. J.R. Macdonald, Impedance Spectroscopy Emphasizing Solid Materials and Systems, John Wiley & Sons, 1987 Chapter 4.
50. Z. Raddaoui, R. Brahem, A. Bajahzar, H.M. Albetran, J. Dhahri, H. Belmabrouk, J Mater Sci **32**, 23333–23348 (2021)
51. I.D. Raistrick, Application of impedance spectroscopy to problems in solid state ionics Solid State Ion. **18**, 40–49 (1986)
52. J.R. Macdonald, Note on the parameterization of the constant-phase admittance element. Solid State Ion. **13**, 147–149 (1984)
53. W. Scheider, B.R. Eisenberg, B.A. Mobley, *Impedance spectroscopy* (Wiley-Inter Science, London, 1975)
54. B.B. Arya, R.N.P. Choudhary, J. Mater. Sci. Mater. Electron. **32**, 11547–11567 (2021)
55. L. Agrawal, B.P. Singh, T.P. Sinha, Mat. Res. Bull. **44**, 1858–1862 (2009)
56. D.C. Sinclair, A.R. West, J. Appl. Phys. **66**, 3850–3856 (1989)
57. K.S. Rao, K.C.V. Rajulu, B. Tilak, A. Swathi, Nat. Sci. **2**, 357–367 (2010)
58. J.K. Lee, H.W. Park, H.W. Choi, J.E. Kim, S.J. Kim, Y.S. Yang, J. Korean Phys. Soc. **47**, 267–270 (2005)
59. A. H. Scott, A. T. McPherson, and Harvey L. Curtis, Rubber Chem. Technol. **7** (1934) 342–370.
60. K. Jonscher, *Dielectric relaxation in solids*, 1st edn. (Chelesa Dielectric Press), London, 1983)
61. H. Hassib, A. Abdel Razik, Solid State Commun. **147** (2008) 345–349.
62. A. Belboukhari, E. Choukri, Y. Gagou, R. Elmoznine, N. Abdelmoula, A. Neqali, M. El Marssi, H. Khemakhem, D. Mezzane, Superlattices Microstruct. **71**, 7–22 (2014)
63. K. Sambasiva Rao, P. Murali Krishna, D. Madhava Prasad, Phys. Status Solidi (b) **244** (2007) 2267
64. F.-C. Chiu, Adv. Mater. Sci. Eng. **647**, 1–18 (2014)
65. X.G. Tang, J. Wang, Y.W. Zhang, H.L.W. Chan, J. Appl. Phys **94**, 5163–5166 (2003)
66. A.K. Jena, S. Satapathy, J. Mohanty, Phys. Chem. Chem. Phys. **21**, 15854–15860 (2019)
67. F.C. Chiu, C.M. Lai, J. Phys. D: Appl. Phys. **43**, 075104 (2010)

**Publisher's Note** Springer Nature remains neutral with regard to jurisdictional claims in published maps and institutional affiliations.

Springer Nature or its licensor (e.g. a society or other partner) holds exclusive rights to this article under a publishing agreement with the author(s) or other rightsholder(s); author self-archiving of the accepted manuscript version of this article is solely governed by the terms of such publishing agreement and applicable law.